

A comprehensive experimental study of the dynamical interaction of He atoms with Cu(001) surface phonons

F. Hofmann and J. P. Toennies

Max Planck Institut für Strömungsforschung, Bunsenstrasse 10, 37073 Göttingen, Germany

J. R. Manson

Department of Physics and Astronomy, Clemson University, Clemson, South Carolina 29634

(Received 26 May 1994; accepted 4 August 1994)

We present new measurements of inelastic He atom scattering from the surface phonons of Cu(001) as a function of crystal temperature, incident energy, and parallel momentum transfer. A careful subtraction of the multiphonon intensity and other background contributions from the time-of-flight intensities reveals three distinct surface-localized vibrational modes which are ascribed to the Rayleigh phonon, the longitudinal bulk resonance, and a further acoustic bulk resonance at higher energy transfers. The longitudinal resonance couples very strongly to the scattering He atoms and, for a wide range of incident conditions, gives peaks which are more intense than those due to the Rayleigh mode. The energy and momentum dependence of these peak intensities are analyzed with the aid of a simple distorted wave Born approximation, and the different coupling parameters for the two modes are determined and compared with other available data. The incoherent diffuse elastic peak is shown to decrease as a function of parallel momentum transfer according to the theory of Fraunhofer scattering from a random array of point defects. The multiphonon background is shown to be in agreement with a quick scattering approximation. © 1994 American Institute of Physics.

I. INTRODUCTION

The first complete measurements by He atom scattering (HAS) of the dispersion curves of close packed face-centered-cubic (fcc)(111) metal surfaces,¹⁻⁴ in addition to mapping out the transverse polarized Rayleigh wave (RW), revealed two unexpected and remarkable features. A second dispersion curve was found which was attributed to a longitudinally polarized resonance (LR) within the bulk phonon band, and this mode under certain conditions had a larger He scattering intensity than the Rayleigh peak. This behavior has been confirmed by recent measurements on the Cu(111) surface.^{5,6} Measurements using electron energy loss spectroscopy (EELS) provide independent confirmation of the dispersion curves on Cu(111). The Cu(001) surface studied in the present article was first examined by Mason and Williams with HAS, but their measurements extended only out to one-half of the Brillouin zone in the $\langle 100 \rangle$ direction.⁷ They were able to clearly distinguish two separate acoustic branches in the phonon dispersion which were tentatively identified as the Rayleigh mode and as the transverse band edge. In 1990, similar results were reported⁸ which also indicated a strong intensity in two surface branches. Recently, the complete dispersion curve of the (001) surface of both Cu (Ref. 9) and Ag (Ref. 10) were measured out to the zone boundary for the $\langle 110 \rangle$ and $\langle 100 \rangle$ symmetry directions by our group in Göttingen. In the $\langle 100 \rangle$ direction, the longitudinal resonance was more than five times more intense on Cu and only about two times more intense on Ag than the Rayleigh mode. Recently, another HAS experiment on the Cu(001) surface has added additional confirmation of the presence of an unexpectedly intense longitudinal resonance.¹¹

The puzzling anomalous aspect of the longitudinal resonance is that, in principle, it should be difficult to detect with HAS because the associated ionic core motion is expected to

be largely polarized in the plane parallel to the surface, yet for a large range of scattering conditions in the $\langle 100 \rangle$ direction, its intensity is much larger than that of the Rayleigh mode. The latter is expected to have the highest excitation probability because its motion is predominantly polarized perpendicular to the surface along the direction with the largest scattering momentum transfer. Deepening the mystery surrounding the behavior of the longitudinal resonance is the inability of EELS experiments reported so far to detect it on the Cu(001) surface.¹²⁻¹⁴

The first careful attempt at a theoretical interpretation of the HAS results for the surface phonons of noble metals was carried out by Bortolani and co-workers.¹⁵⁻¹⁷ They used a Born-von Kármán theory approach based on a parametrization of the force constants, and were able to explain both the Rayleigh mode and the longitudinal resonance for the (111) surfaces of Ag,¹⁶ Au,¹⁸ and Pt.¹⁹ They calculated time-of-flight spectra for direct comparison with the experimental data assuming a pairwise summation of two body repulsive interactions of the He atoms with the surface metal atoms. In order to obtain satisfactory fits of the peak location and intensities in the time-of-flight spectra, they had to significantly weaken the force constants at the surface and between the surface and the subsurface layer in order to obtain eigenvectors of the longitudinal mode with the significant vertical polarization needed to fit the longitudinal mode intensity. In particular, the radial force constant between atoms within the surface plane had to be softened by up to 70%, an amount which is difficult to reconcile with the fact that these close-packed surfaces do not reconstruct and exhibit almost negligible relaxation. In contrast, a similar Born-von Kármán theoretical approach to the Cu(111) surface carried out later by Mills and co-workers was able to explain all of the dispersion curves obtained with the EELS experiments with

only a modest and acceptable softening of the surface radial force constants by a factor of about 30%.^{20,21} However, this force constant model with the same two body interaction potential used previously cannot account for the strong coupling to the longitudinal resonance^{1,2,5} observed in HAS.

Recently a semiempirical pseudocharge model has been introduced which is able to explain all the HAS results.^{5,6} The pseudocharge model is an outgrowth of early attempts to account for the dynamical coupling of the cores to the electrons occurring in bulk vibrations of insulators and semiconductors. The early shell model of Cochran²² with further developments by Phillips,²³ Martin,²⁴ and Weber^{25,26} was first applied to metal surfaces by Jayanthi, Bilz, and Benedek.²⁷ In these models, the coupling of the lattice to the electrons is accounted for by including charges either concentric with the ion cores as in the shell models or between the ion cores. To satisfy the adiabatic condition, the mass of the charges is considered negligible compared to that of the cores. In the pseudocharge model, the distortion of the charges is expanded in spherical harmonics, hence it is also called the multipole expansion model.^{5,6,27} The distortion of the charge clouds gives rise to additional interactions between the atoms of the lattice. At the surface, the distortions induced by the surface atom motion parallel to the surface can modulate the weak surface electron density (10^{-4} e/a.u.³) in the vertical direction at distances of 7–9 a.u. above the surface layer of atoms where the He atoms interact with the surface. Since the repulsive He-surface potential is roughly proportional to the surface electron density, this provides a mechanism by which the He atoms can effectively couple to the longitudinal resonance.²⁸ This multipole expansion pseudocharge approach has been very successful in explaining the dispersion curves as well as the measured intensities of the longitudinal resonance measured by HAS for both Cu(111) and Cu(001).^{5,9} The theory reveals that the excitation of the transverse polarized Rayleigh mode is correctly described by the summation of two body repulsive potentials as in the theory of Bortolani and co-workers. The softening of the effective surface radial force constant required to fit the data is $\sim 30\%$, which is reasonably consistent with the Born–von Kármán force constants used to explain the EELS data.^{21,29}

The phenomenological nature of the pseudocharge model points out the need for first principles calculations. A first principles, total electronic energy approach has been put forward by Ho and Bohnen.^{30,31} The calculations are performed using the norm-conserving first principles pseudopotential approach within the local density functional formalism. Surface force constants can be calculated only at high symmetry points in the Brillouin zone, and the dispersion curves for the entire zone are obtained in a standard Born–von Kármán dynamical matrix calculation. The frequencies at the \bar{X} and \bar{M} points of the surface Brillouin zone of Cu(001) (Ref. 29) and the complete set of dispersion curves of Cu(111) are found to be in good agreement with the EELS^{32,33} and HAS dispersion curves. However, calculations of the anomalously large intensities of the longitudinal resonance have not been reported so far. Calculations of HAS intensities have also not been reported in other theoretical approaches based on the effective medium theory.^{34–36}

Recently the Trieste group has put forward a related phenomenological model which also provides good agreement with some of the available data for both elastic diffraction and inelastic He scattering from Cu surface.¹¹ In principle, this model is consistent with the earlier work of Bortolani and co-workers in that the phonon spectrum is calculated within the Born–von Kármán constant theory, and the interaction between the He atoms and the surface is represented by a pairwise sum of potentials. The difference is that the potentials are a parametrized combination of repulsive cores which are flattened into ellipsoidal shapes with the large axes parallel to the surface plane combined with attractive van der Waals terms. The use of these flattened potentials gives rise to a smoother surface potential for elastic scattering than would be expected by using a pairwise summation of spherical potentials, and calculated diffraction patterns agree well with HAS angular distributions.¹¹ For inelastic scattering, the motions of the conduction charges are modeled by the overlap of the flattened potentials between the ionic cores in a manner very similar to that of the multipole expansion pseudocharge model.

In order to have a basic set of data for a more discriminating test of these new theories, we have carried out more extensive HAS measurements of the dispersion curves and inelastic scattering intensities from the Cu(001) surface. In the following section, we present a brief description of the apparatus. In Sec. III, we present the experimental results and the experimental time-of-flight spectra. The dependence of phonon inelastic peak intensities are reported for the $\langle 100 \rangle$ and the $\langle 110 \rangle$ symmetry directions out to the Brillouin zone boundary over a wide range of incident He beam energies E_i (20–112 meV) and crystal temperatures T_S (110–1000 K). Section IV describes the procedures used to analyze the data, especially the deconvolution of the time-of-flight spectra. In Sec. V, the results of this evaluation are then presented. The Rayleigh and longitudinal intensities show a different behavior in many respects, suggesting that the He coupling mechanism is indeed different for the two modes. In Sec. VI, the basic theory is outlined, including that used in the multiphonon analysis of the data. Finally a discussion of the results is given in Sec. VII.

II. APPARATUS

Figure 1 shows a simple schematic diagram of the time-of-flight apparatus with the essential components and definitions of some important parameters. This apparatus, designated HUGO II, is a modified version of one described in detail in an earlier Ref. 37. An extensive compilation of the relevant operating parameters and dimensions is collected in Table I. The atomic beam of helium is formed by an adiabatic expansion from a high pressure (≈ 400 bar) through a cylindrical orifice with a diameter of 10 μm . The source is attached to a closed cycle helium refrigerator and can be heated resistively, so that its temperature can be varied continuously from 25 to 700 K. This corresponds to beam energies in the range of 5 up to 140 meV. The beam then passes through a commercial conical skimmer³⁸ (diameter of opening = 0.68 mm) and three vacuum chambers, one of which contains the rotating disk copper for time-of-flight

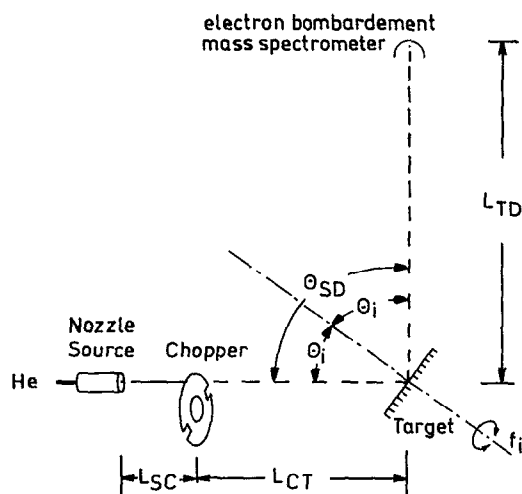


FIG. 1. A schematic diagram showing the essential components and definitions of the important angles and distances of the HUGO II scattering apparatus.

measurements (see Table I) before entering the ultrahigh vacuum (UHV) target chamber, which houses the crystal and the equipment (sputter gun, cylindrical mirror Auger spectrometer, and LEED) for metal surface preparation and characterization. In addition, a mass spectrometer is provided for residual gas analysis. The scattered atoms are detected by a

magnetic sector field mass spectrometer, which is located at 1.4 m from the target at a fixed angle of $\theta_i + \theta_f = 95.8^\circ$ with respect to the incident beam direction.

The sample is mounted on a manipulator providing x , y , and z translations as well as rotations about three axes. The polar angle θ of the manipulator can be adjusted to within $\Delta\theta \leq 0.05^\circ$ as required by the small detector in-plane acceptance angle of $\approx 0.2^\circ$. The target holder is provided with an electron bombardment heater and a liquid N_2 or He cooling arrangement, which allows for crystal temperatures in the range of 50 up to 1200 K. The Cu(001) crystal surface was oriented to better than 0.2° , mechanically polished, and further prepared by repeated cycles of sputtering (800 eV Ar^+ ions at 500 K) and annealing at 850 K for 10 min. No contamination above 1% could be detected by Auger analysis.

The detector consists of an electron bombardment ionizer followed by the magnetic sector field mass analyzer. The detector design is optimized for use with light particles. For He, a detector sensitivity of 3×10^{-6} ions per incident atom (at $E_i = 66$ meV) is achieved within an active area of 4×8 mm² and 5 mm length.

To suppress the background signal, the He partial pressure rise in the detector chamber resulting from the pressure rise in the source chamber is reduced by extensive differential pumping along the flight path. In addition to the three differential pumping stages situated between the source and target chamber, four additional pumping stages are located between the target chamber and detector chamber. Including

TABLE I. Relevant operating parameters and important dimensions of the HUGO II apparatus.

Source	Nozzle-orifice diameter d , nominal	10 μ m
	Nozzle stagnation pressure	1–400 bar
	Nozzle stagnation temperature	25–700 K
	He-beam energy	5–140 meV
	Relative velocity spread $\Delta v/v$ (FWHM)	0.01
	Estimated intensity	3×10^{19} atoms/sr/s
Skimmer (Ref. 38)	Entrance diameter	0.68 mm
	Length; entrance to base	25.4 mm
	Outside/inside included angles at orifice	30°/25°
	Orifice-to-skimmer distance	18 mm
Chopper	Double-slit disk, minimum and maximum radius of slits	71–84 mm
	Slit widths at minimum and maximum radius	5–1 mm
	Disk rotational frequency	100–500 Hz
	Shutter function (FWHM), effective	110–4 μ s
Dimensions	Source-target distance $L_{SC} + L_{CT}$	675 mm
	Target-detector distance L_{TD}	1402 mm
	Chopper-detector distance $L_{CT} + L_{TD}$	1984 mm
	Source-target-detector angle θ_{SD}	95.8°
	Incident-beam full angular spread, nominal	0.66°
	Angle subtended by detector from target, nominal	0.17° (in plane), 0.35° (out of plane)
Pressures	Angular resolution (in plane), (00) peak, nominal	0.68°
	Angular resolution (in plane), (00) peak, measured	0.33°
	Target chamber	
	Base	8×10^{-11} mbar
	Operation, beam chopped	1×10^{-9} mbar
	Operation, beam unchopped	1×10^{-7} mbar
Detector chamber		
Base	6×10^{-11} mbar	
Operation, beam chopped, specular	1×10^{-10} mbar	
Operation, beam unchopped, specular	1×10^{-8} mbar	

the pumps in the source, target, and detector chambers, there are altogether ten pumping stages. Under unchopped beam conditions, the residual He partial pressure is reduced from 10^{-3} mbar in the source chamber down to 10^{-7} mbar in the target chamber and to 10^{-13} mbar in the detector chamber (crystal removed from the beamline). In the time-of-flight mode (chopped beam), the He intensities and partial pressures are further reduced by a factor of 100. Signals ranging from 5 counts/s (background) up to about 10^9 counts/s (incident beam intensity) can be measured.

The overall energy resolution, which is determined by the velocity smearing of the He beam, the chopper opening time, the axial detector length, and the kinematical conditions,³⁹ has been estimated to be $\Delta E = 0.65$ meV [full width at half-maximum (FWHM)] for the specular beam under typical measuring conditions of $E_i = 30$ meV, a value which has been confirmed experimentally. Such a relative resolution of $\Delta E/E = 2\%$ can be achieved for energies up to 60 meV. The resolution decreases at higher energies since the nozzle pressure required to maintain the 2% resolution increases rapidly with the nozzle temperature, and the corresponding flux would exceed the effective pumping speed of 4500 ℓ/s of the nozzle chamber diffusion pump. For typical phonon measurements, however, this is not a restriction, as will be shown in the following section.

III. EXPERIMENTAL MEASUREMENTS

An overview of the time-of-flight (TOF) spectra taken along the $\langle 100 \rangle$ direction is shown in Fig. 2. These and the results along the $\langle 110 \rangle$ direction are in complete agreement with the earlier data,⁹ shown for comparison in Fig. 3 obtained from another apparatus (Gurke).

Besides the incoherent elastic peak at $\Delta E = 0$ meV, all spectra show two sharp inelastic peaks, which are attributed to the predominantly vertically polarized Rayleigh wave mode and the longitudinal resonance. They are superimposed on a broad inelastic background, which is due mainly to multiphonon scattering events, as will be demonstrated in Sec. IV. Whereas the width δ of the RW peak corresponds solely to the experimental energy resolution, the LR peak is additionally broadened by about $\delta_L = 0.25$ meV.⁴⁰ In some spectra, e.g., at $\theta_i = 38.9^\circ$, there is evidence for a third even broader inelastic peak with energy losses larger than that corresponding to the longitudinal resonance. In addition, a weak peak is observed with $\Delta E = -1.7$ meV at angles close to the specular. This peak has been identified as an artifact caused by reflections of the very intense He pulses within the ionization region of the detector.

The LR peak is expected to be broadened by the coupling to the bulk bands with the same polarization and phonon energies and wave vectors. Thus the phonon spectral density of the LR is, in fact, made up of a band of modes, while the RW is a single isolated mode, which for a perfectly ordered and infinite surface, appears as a δ function in the spectral density at a given energy for each value of ΔK in the Brillouin zone. Therefore we expect the measured width of the LR peak to be larger than that of the RW, as is observed. An additional contribution to the increased width of the LR peak is related to the fact that it has in addition to the pre-

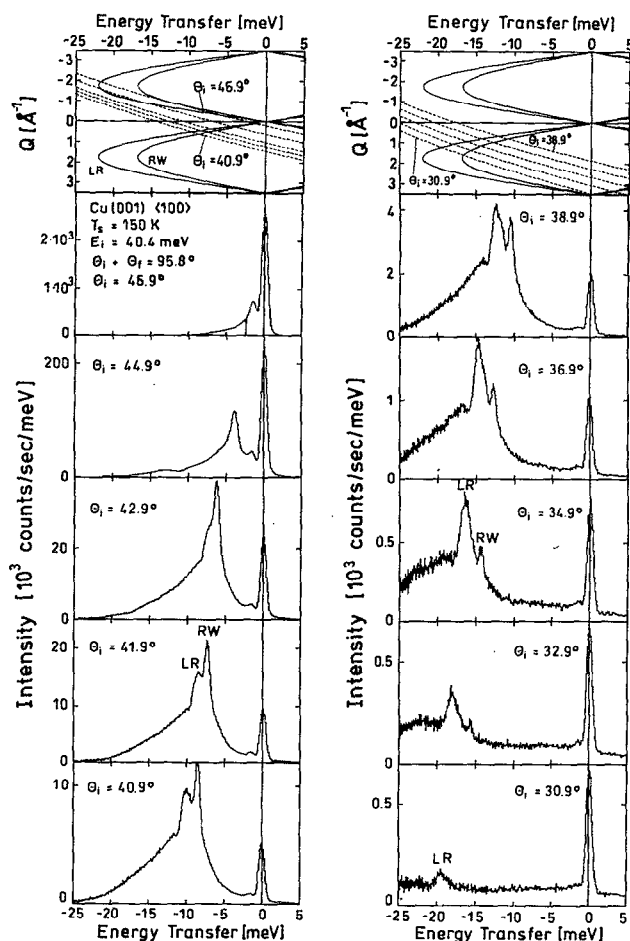


FIG. 2. A series of TOF spectra transformed to an energy transfer scale taken along the $\langle 100 \rangle$ azimuth for ten different incident angles θ_i . The crystal temperature is $T_s = 150$ K and the incident energy is $E_i = 40.4$ meV. For identifying the individual TOF peaks, the corresponding scan curves for forward-creation inelastic scattering (dashed lines) and an idealized phonon spectrum for the RW and LR (solid lines) are shown at the top.

dominantly parallel vibrational amplitude also a perpendicular component. At a given ΔK value, the maximum in the amplitude arises at slightly different energies for these two different polarizations.⁴¹

In Fig. 2, the scattered intensities are given in units of counts/second per millielectron volt energy loss. The intensities from different time-of-flight spectra can be compared without further correction since the incident beam intensity was constant to within 2% for all measurements. The peak intensities decay very rapidly with decreasing incident angle corresponding to larger parallel momentum transfer. As a result, the spectrum at $\theta_i = 46.9^\circ$ took only 5 min to obtain, whereas the spectrum at $\theta_i = 30.9^\circ$ required 2 h. At small incident angles, the intensity due to the longitudinal resonance becomes increasingly dominant. In fact, in the measurement taken at $\theta_i = 30.9^\circ$, the RW intensity has vanished completely, whereas the longitudinal resonance is still clearly visible. Due to the rapid intensity decay at smaller angles, we

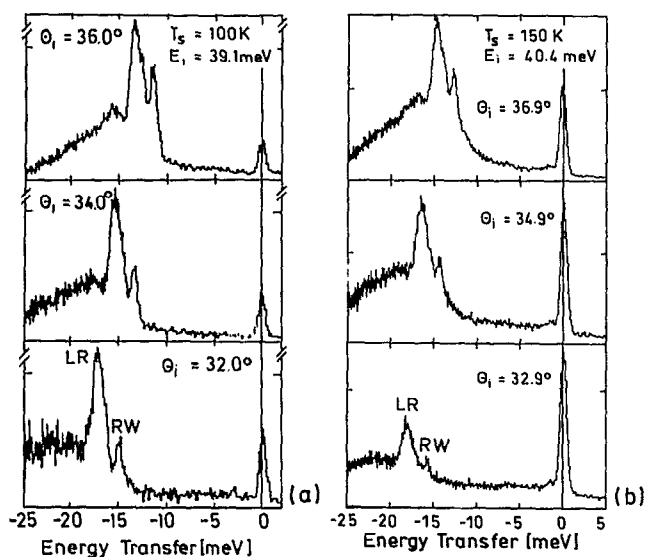


FIG. 3. Two series of TOF spectra taken under comparable kinematical conditions with two different crystals in two different machines. (a) Data taken from Ref. 9 ($T_S=100$ K, $E_i=39.1$ meV) measured in the fall of 1990. (b) The new data ($T_S=150$ K and $E_i=40.4$ meV). Both series show complete agreement for the intense inelastic contribution due to the longitudinal resonance. The difference in the incoherent elastic intensity reflects differences in the defect concentration on the two crystal samples which happened to be present during the respective measurements.

were not able to observe both single phonon peaks at momentum transfers close to the Brillouin zone edge with the incident energy of $E_i=40.4$ meV. However, by increasing the incident energy to $E_i=83.2$ meV and using kinematical conditions corresponding to creation events with negative parallel momentum transfer ($\Delta K < 0$), the TOF spectra show clearly resolved energy loss peaks corresponding to momentum transfers up into the second Brillouin zone, as is shown in Fig. 4.

The corresponding series of TOF spectra along the $\langle 110 \rangle$ direction is shown in Fig. 5. As observed previously,⁹ the intensity of the longitudinal resonance is considerably weaker in this direction and is always much smaller than the RW inelastic intensity.

In order to examine the temperature dependence of the different contributions to the scattered intensity, TOF spectra were measured along the $\langle 100 \rangle$ direction at crystal temperatures in the range from 115 up to 800 K for several different fixed incident angles. In Fig. 6, we show a series of TOF spectra for an incident angle of $\theta_i=39.9^\circ$. For all temperatures at this angle, the RW ($\Delta E=-8.0$ meV, $\Delta K=0.56 \text{ \AA}^{-1}$) and LR peaks ($\Delta E=-9.3$ meV, $\Delta K=0.39 \text{ \AA}^{-1}$) remain at the same respective energy losses and the RW peak is always more intense than the LR peak. Thus the main effect of increasing the temperature is to increase the broad background due to multiphonon scattering. Even at temperatures as low as 110 K, the integrated intensity of the broad background is the dominant contribution to the scattered intensity as is discussed in Sec. V C. Although it would appear from the spectra shown in Fig. 6 that the LR increases with respect to the RW with increasing temperature, this is not in

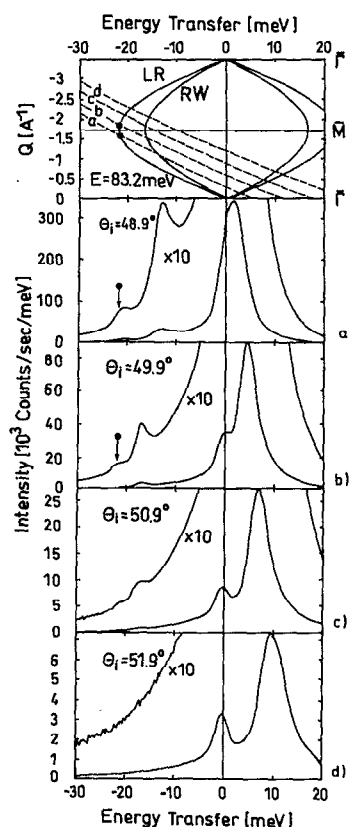


FIG. 4. A series of TOF spectra converted to the energy transfer scale with an incident energy of 83.2 meV. The surface temperature is 111 K. The topmost panel shows the corresponding scan curves, where it is seen that the energy transfer corresponds to momentum transfers of both the LR and RW modes up to the Brillouin zone edge and beyond.

fact the case as a more careful analysis presented in Sec. IV shows. At 800 K, there is no longer a diffuse elastic contribution due to Debye–Waller attenuation, and the two single phonon peaks have merged into one unresolved broader peak which has an energy loss closely equal to that of the single phonon LR peak. A second series was measured at a smaller incident angle of $\theta_i=31.8^\circ$ and is shown in Fig. 7. Here the LR intensity ($\Delta E=-15.64$ meV, $\Delta K=-0.78 \text{ \AA}^{-1}$) dominates in comparison to the RW intensity ($\Delta E=-13.9$ meV, $\Delta K=1.05 \text{ \AA}^{-1}$). Again the increase of the LR intensity in comparison to the RW is only apparent and not real. The main effect of increasing the temperature is again a strong enhancement of the multiphonon background intensity. Here as in Fig. 6 there is no evidence for any shift or broadening of the single phonon peaks with crystal temperature within the experimental accuracy, which is estimated to be $\delta(\Delta E) \leq 0.05$ meV.

Next we describe measurements of the dependence of the scattered intensities on the incident energy of the He atoms. The interpretation in this case is less straightforward since the kinematical conditions change with incident energy. This can be compensated for by adjusting the incident angle so that the scan curve passes through the same point in the $(\Delta E, \Delta K)$ plane. One set of TOF spectra taken with incident energies in the range from $E_i=20.1$ up to 73.5 meV is

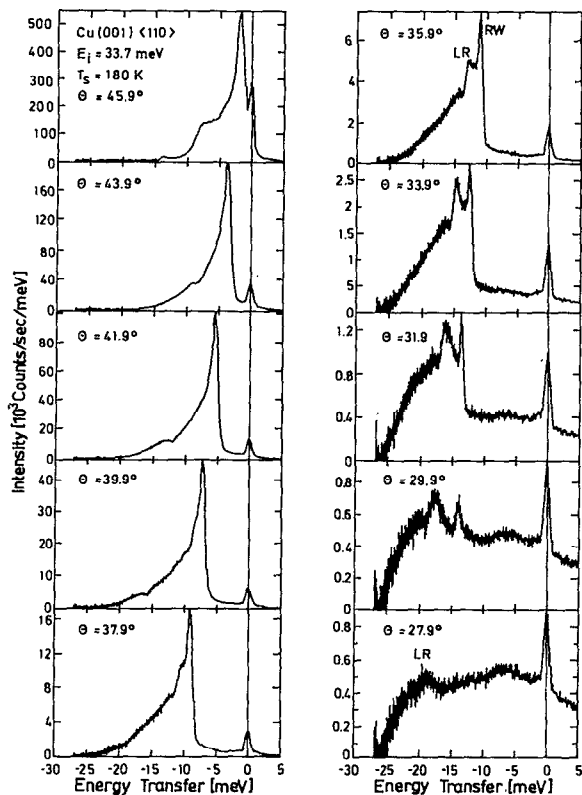


FIG. 5. The same as Fig. 2, but along the $\langle 110 \rangle$ direction and at a crystal temperature of $T_S = 180$ K.

shown in Fig. 8. The nozzle pressure is adjusted for each incident energy to obtain an optimum resolution. The kinematic conditions of all spectra are chosen to cross the dispersion curve of the Rayleigh mode at $\Delta E = -7.8$ meV, and $\Delta K = 0.56 \text{ \AA}^{-1}$, where the RW mode dominates. The broadening of the peak with increasing beam energy is due simply to the fact that the absolute experimental energy resolution is nearly proportional to the beam energy.

A second series of TOF spectra as a function of energy is shown in Fig. 9, where the scan curves intersect close to the longitudinal resonance at $\Delta E = -15.8$ meV and $\Delta K = 0.81 \text{ \AA}^{-1}$. In Figs. 8 and 9, it is not possible to compare directly the intensities in the different TOF spectra since they depend on the incident angle and the nozzle pressures. A procedure to correct for these influences is presented in the following section. However, even without a quantitative analysis, it is obvious from the spectra that the multiphonon intensity grows with the incident energy at the expense of the incoherent elastic intensity and the single phonon events.

IV. DATA EVALUATION

The physical quantity of interest in these results is the differential reflection coefficient $d^3R/dE_f d\Omega_f$, which we measure for elastic scattering, single phonon scattering by the RW mode, the longitudinal resonance, and other sharp features, as well as the broad background which we attribute

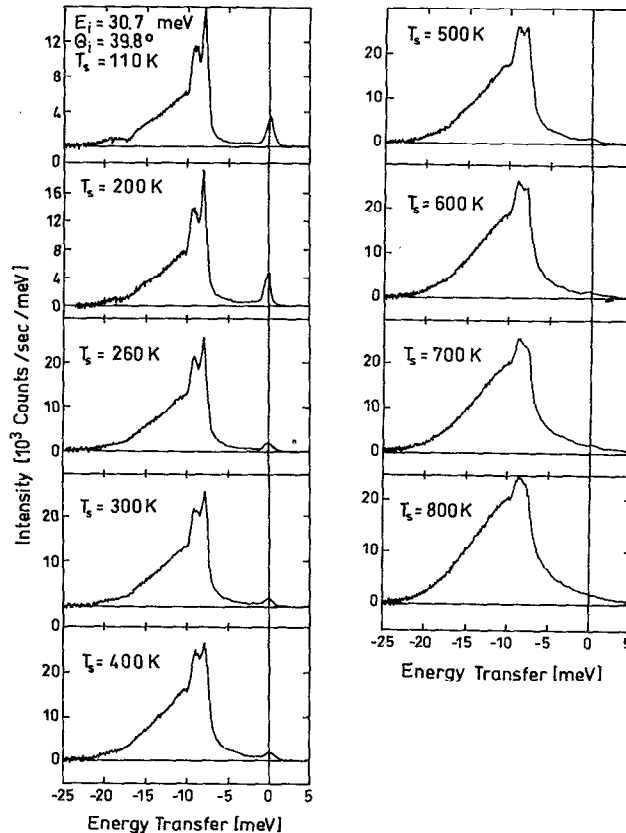


FIG. 6. Crystal temperature dependence from $T_S = 110$ to 800 K of TOF spectra taken along $\langle 100 \rangle$ with incident energy $E_i = 30.7$ meV and incident angle $\theta_i = 39.8^\circ$.

mainly to multiphonon scattering. As a first step, we extract the different contributions with the aid of a simple fitting procedure assuming a Gaussian function for each structure. The intensities obtained in this way are then corrected in a second step for the different experimental parameters.

A. Deconvolution of the TOF spectra

The deconvolution of the spectra into different contributions is based on the assumption that their shape can be described by Gaussians. This assumption can be justified³⁹ for the incoherent elastic and the single phonon intensities, including the slightly broadened LR, because these peak widths are largely determined by the experimental resolution. In this case, Monte Carlo simulations confirm a Gaussian-like peak shape.³⁹ The shape of the broad background, however, is much less obvious. As we also expect, a nearly Gaussian distribution for the multiphonon scattering contribution⁴² (see also Sec. VI), we first attempted to fit the background with a single Gauss function. To obtain a good fit close to the center of the multiphonon contribution, however, we had to include a fourth inelastic peak, which was assumed to be a Gaussian. Figure 10 shows a typical example of a spectrum deconvoluted in this way. The broad Gaussian, labeled (d) and centered at -12 meV, is attributed to multiphonon processes. In addition to the incoherent elastic peak labeled (a) at 0 meV and the two single phonon

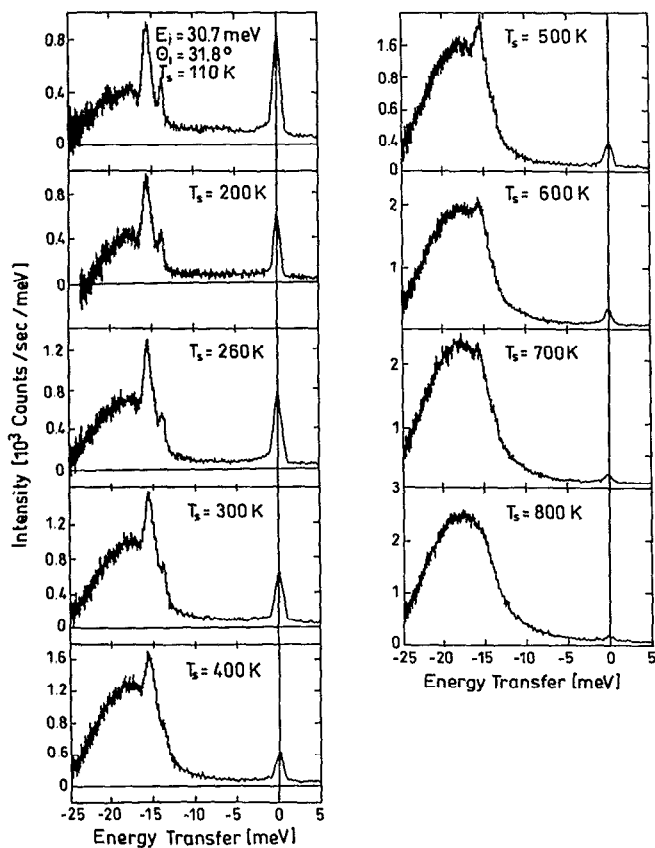


FIG. 7. Crystal temperature dependence from $T_S=110$ to 800 K of TOF spectra taken along (100) with incident energy $E_i=30.7$ meV and incident angle $\theta_i=31.8^\circ$.

peaks (b) and (c) due to the RW (-7.5 meV) and the LR (-9 meV), respectively, there is a contribution (e) at -10 meV, which is much narrower than the multiphonon background, but considerably broader than the experimental resolution. We attribute this additional contribution, on the basis of its temperature dependence, to single phonon exchange with the continuum of bulk projected modes.

Since the decomposition procedure, especially the handling of the background, is essential for the interpretation presented in the next section, we performed a consistency check with a theoretical analysis of the multiphonon contribution. Figure 11 shows a comparison of the measured temperature dependence of the integrated multiphonon intensity (peak d) with the theoretical results to be described in Sec. VI. The agreement between theory and experiment is very good. The width (FWHM) of the multiphonon peak shown in Fig. 12 and the position are nearly independent of the surface temperature. Both are in good agreement with theory.⁴³ Moreover, the Debye–Waller factors of the bulk and single surface phonon contributions show the expected different behavior as discussed in Sec. V. These observations provide convincing evidence for our assignment of the multiphonon background.

An even more direct check of the temperature dependence of the TOF spectra can be obtained by looking at the

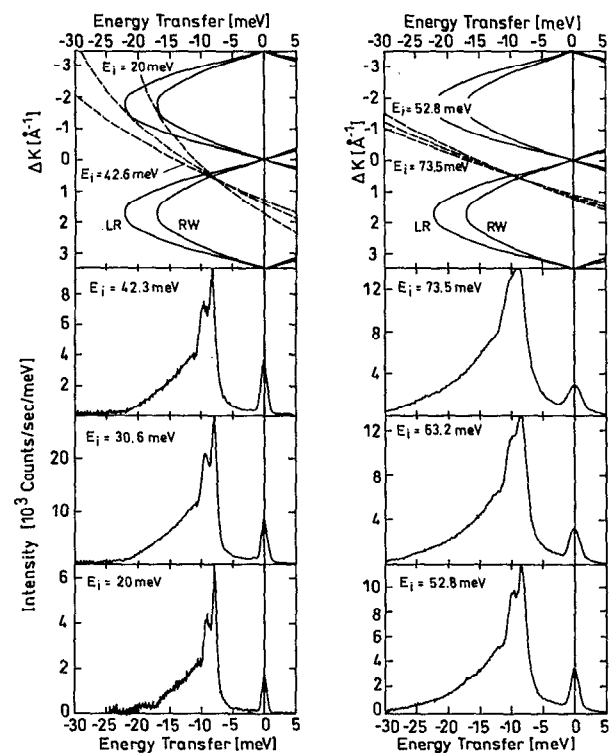


FIG. 8. TOF spectra taken along (100) converted to an energy transfer scale for different incident energies in the range from $E_i=20.1$ up to 73.5 meV. In addition to the TOF spectra, the corresponding scan curves are displayed at the top. The crystal temperature is $T_S=110$ K. All scan curves intersect on the RW dispersion curve at the same point $\Delta E=-7.8$ meV and $\Delta K=0.56 \text{ \AA}^{-1}$.

difference function of a TOF intensity at higher T taken with respect to the low temperature spectrum which would be measured ideally in the limit of 0 K. Figure 13 shows as an example the difference spectrum between a measurement at $T_S=200$ K and a reference spectrum at $T_S=110$ K, after subtracting the multiphonon background from each. Changes in the different contributions due to single phonons and incoherent elastic scattering are easily identified. All of the peaks are positive, which is expected for the inelastic contributions in that temperature range because of the increasing Bose occupation number (see Sec. V). The incoherent elastic peak would normally be expected to decrease with temperature and appear as a dip in the difference spectrum. However, this contribution is extremely sensitive to the presence of defects, which may explain why it appears as a positive peak. Very importantly, a new single phonon peak attributed to the bulk resonance “2” shows up as a sharp structure in the difference spectrum at -11 meV. Such a mode was previously identified through extensive comparisons with theory on Al(001),⁴⁴ where it was designated as mode 2. The theory attributes this contribution to a small maximum in the transverse vertical polarized density of bulk states.^{44,45} This provides additional confirmation that the peak has been correctly interpreted and is not, e.g., an artifact arising from an incorrect subtraction of the multiphonon background. This

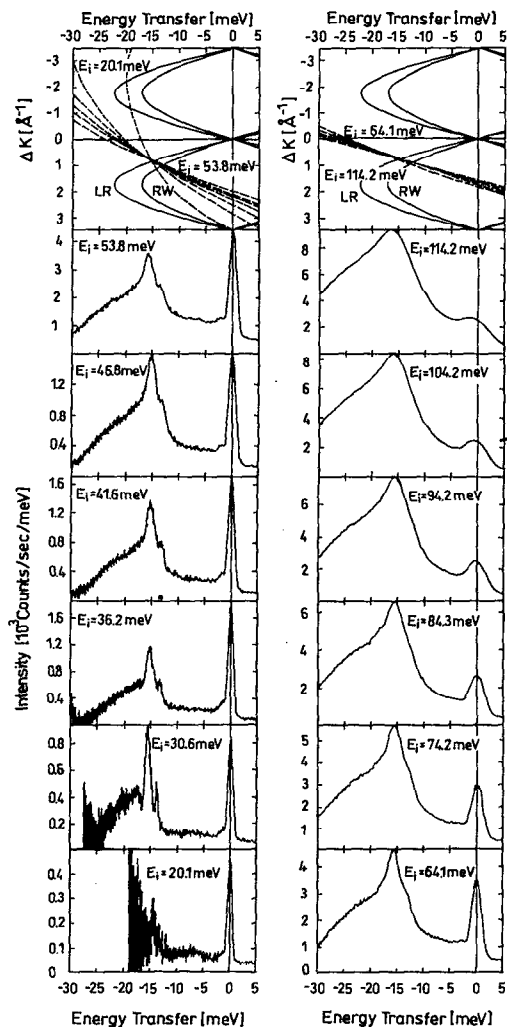


FIG. 9. TOF spectra taken along $\langle 100 \rangle$ converted to an energy transfer scale for different incident energies in the range from $E_i = 20.1$ up to 114.2 meV. The crystal temperature is $T_S = 110$ K. In addition to the TOF spectra, the corresponding scan curves are displayed at the top. All scan curves intersect the LR dispersion curve at the same point $\Delta E = -15.8$ meV and $\Delta K = 0.81 \text{ \AA}^{-1}$.

and other possible explanations for this peak are discussed in Sec. VII.

B. Corrections due to experimental parameters

The measured intensities have to be corrected for the following experimental parameters. (1) Changes in the flux through the nozzle with changing source conditions. This is taken into account by normalizing the measured intensities by the pressure rise in the target chamber. The pressure rise is a direct measure of the beam flux on the crystal since the pumping speed is constant at the small pressures involved. (2) A change in detector sensitivity with beam velocity. The detector is sensitive to the beam density, and therefore to obtain the corresponding flux, the measured count rates should be corrected by dividing with a factor of $1/v_f$ where v_f is the final velocity. The data presented here does not include this correction; rather it was included in the theoretical output when comparing with the experimental data. (3)

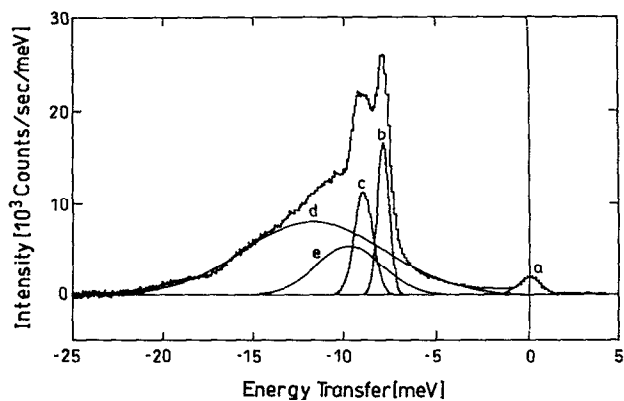


FIG. 10. Deconvolution scheme for measured TOF spectra. Shown is a measured TOF spectrum at $T_S = 110$ K in the $\langle 100 \rangle$ azimuth ($E_i = 30.6$ meV, $\theta_i = 39.8^\circ$) and the five Gaussians labeled (a)–(e), fitted to the spectrum as explained in the text.

Kinematical conditions; the measured intensities were corrected for different amounts of kinematic focusing resulting from the different scan curve conditions and the angles at which the scan curves intersect the dispersion curves.³⁹ (4)

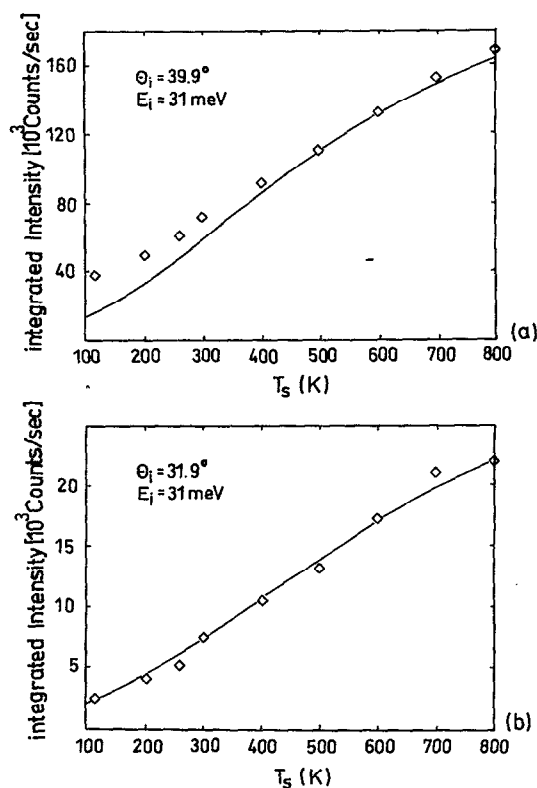


FIG. 11. A comparison of the measured temperature dependence of the integrated multiphonon intensity with theory for $E_i = 31$ meV. The experimental points were obtained by a Gaussian fit of peak (d) (see Fig. 10) of the TOF spectra, as discussed in Sec. IV, and the theoretical curve was calculated from Eq. (14) with $\Theta_D = 280$ K. (a) $\theta_i = 39.9^\circ$, $\beta = 2.9 \text{ \AA}^{-1}$, and $Q_C = 1.0 \text{ \AA}^{-1}$, and (b) $\theta_i = 31.9^\circ$, $\beta = 4.9 \text{ \AA}^{-1}$, and $Q_C = 0.95 \text{ \AA}^{-1}$.

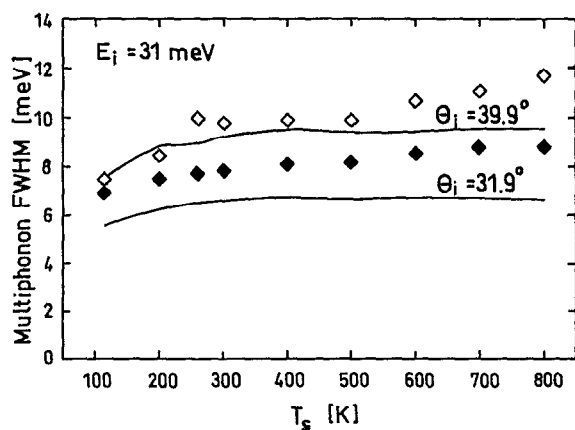


FIG. 12. A comparison of the temperature dependence of the measured multiphonon peak width (FWHM) with theory for $E_i=31$ meV, $\theta_i=39.9^\circ$ (upper curve), and $\theta_i=31.9^\circ$ (lower curve). The experimental points were obtained by a Gaussian fit of peak (d) (see Fig. 10) of the TOF spectra as discussed in Sec. IV, and the theoretical curves were calculated from Eq. (14) with the parameters used for Fig. 11.

Changes in the crystal area illuminated by the impinging He beam and area seen by the detector for different scattering angles. The former two corrections are especially important for the measurements of the energy dependence of the intensities. The latter two factors, however, turned out to have only a small influence.³⁹

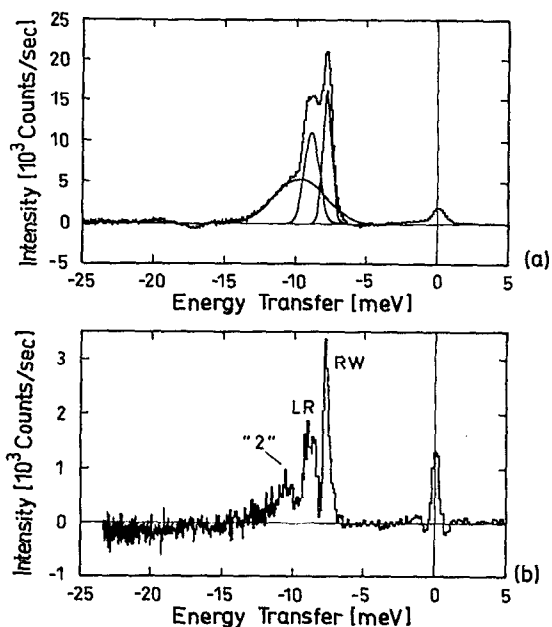


FIG. 13. (a) The same TOF spectrum as in Fig. 10 ($E_i=30.6$ meV, $\theta_i=39.8^\circ$, $T_s=110$ K, and $\langle 100 \rangle$ azimuth) with the multiphonon background subtracted. (b) The difference spectrum between a measurement at $T_s=200$ K and the spectrum shown in (a). The positive peaks are due to the Bose occupation number enhancement of the inelastic scattered intensity. The difference spectrum confirms the existence of three peaks in the TOF spectrum.

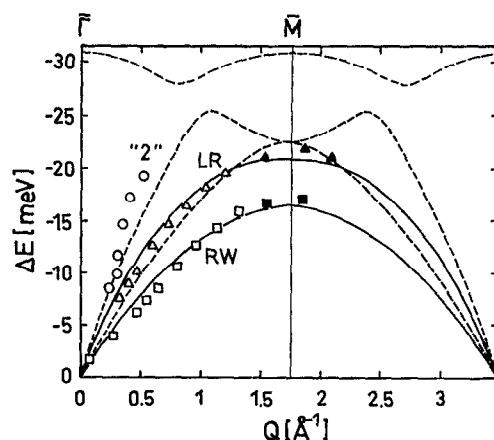


FIG. 14. Measured dispersion curves of the RW mode and the LR of Cu(001) along the $\langle 100 \rangle$ symmetry direction: (Δ) LR; (\square) RW mode, and (\circ) mode "2." The solid lines are pseudocharge calculations taken from Benedek *et al.* (Ref. 9). Open data points taken at $E_i=40.4$ meV and filled data points taken at $E_i=83.2$ meV. The dashed lines show the boundaries of the projected bulk bands.

V. RESULTS

A. Dispersion curves

The dispersion curves for the Rayleigh mode and the longitudinal resonance obtained from the single phonon energy transfers and corresponding momentum transfers from all of the measured TOF spectra as described in Ref. 37 are shown in Fig. 14. The RW mode and the LR could be traced out over the entire first Brillouin zone and even somewhat beyond. The observed zone edge energies are $\hbar\omega=17.1$ meV for the RW mode and $\hbar\omega=21.8$ meV for the LR.

B. Parallel momentum dependence

The dependence of the intensities of the elastic peak and of the single phonon peaks due to the RW mode and the LR on the parallel momentum transfer is shown in Fig. 15. The dependence of the diffuse elastic peak on parallel momentum transfer provides significant information concerning the elastic differential cross section for scattering of He atoms from the defects which lead to this contribution.⁴⁶ Since as shown below the number of steps on the target crystal is quite low, the defects are expected to be predominantly pointlike,⁴⁶ i.e., adsorbates, adatoms, or vacancies. Very near to the specular beam at small parallel momentum transfer $\Delta K \approx 0$, such point defects have a very large differential cross section due to the long-range van der Waals attractive potential. This contribution falls off rapidly with increasing ΔK , and at angles further away from specular, the Fraunhofer contribution from the hard core repulsive part of the defect potential dominates. An estimate of this behavior can be obtained by assuming that the hard core repulsion of a typical defect is axially symmetric and subtends a radius a on the surface. The Fraunhofer reflection coefficient is then the same as that of a hole of radius a , which to a good approximation is $|J_1(\Delta K a)/\Delta K a|^2$, where $J_1(x)$ is the Bessel function of order unity.⁴⁶ This reflection coefficient decays with ΔK ac-

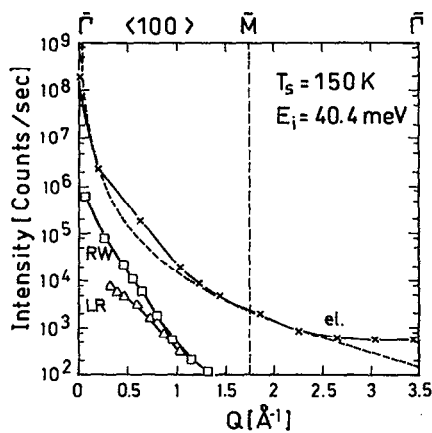


FIG. 15. Measured intensities of single phonons and of the diffuse elastic peak as a function of parallel wave vector transfer; diffuse elastic (\times), Rayleigh mode (\square), and longitudinal resonance (\triangle). The dashed curve is the theoretical Fraunhofer envelope for the diffuse elastic scattering from point defects (Ref. 46). The solid lines are drawn through the experimental points to guide the eye.

According to the envelope function $1/\Delta K^3$ which is independent of a . Thus the envelope function remains the same even if there is a distribution of different defects with different radii. Therefore, if the diffuse elastic contribution is from point defects, we would expect to see a decay consistent with the $1/\Delta K^3$ envelope, as opposed to a $1/\Delta K^2$ envelope expected for step edges normal to the sagittal scattering plane. The theoretical curve shown in Fig. 15 is the Fraunhofer $1/\Delta K^3$ envelope multiplied by the necessary factors to convert it into a differential reflection coefficient.⁴⁷ For defects with hard core radii in the 2–3 Å range as expected here, the Fraunhofer contribution becomes smaller than the direct or illuminated face scattering from the hard core for values of $\Delta K \geq 3-4 \text{ \AA}^{-1}$.⁴⁶ The direct hard core scattering contribution from an isolated defect has an envelope which is nearly independent of ΔK .⁴⁶ Consequently, this hard core contribution from a distribution of defect sizes should be independent of ΔK . The fit with the diffuse elastic data points is very good over the entire measured range, except at the largest values of ΔK , where the Fraunhofer curve seems to be below the data points. This could indicate the onset of the region where the illuminated face contribution is dominant. The good agreement between the diffuse elastic contribution and the Fraunhofer envelope indicates that the surface defects observed here are indeed point defects.

The momentum transfer dependence of the single phonon scattering contains information about the range of the repulsive dynamical coupling potential between the He atom and the surface,⁴⁸ which is discussed in Sec. VI A following a description of the theory.

C. Temperature dependence

A systematic analysis of the Debye–Waller behavior of the different total integrated elastic and inelastic contributions to the TOF intensities is shown in Fig. 16 for

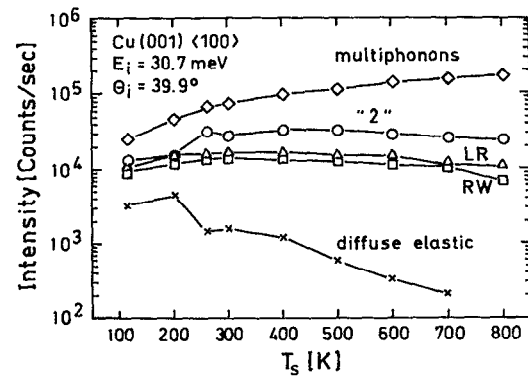


FIG. 16. Measured dependence on surface temperature in the $\langle 100 \rangle$ azimuth of RW (\square), LR (\triangle), multiphonons (\diamond), diffuse elastic scattering (\times), and the single phonon resonance 2 (\circ) for $\theta_i = 39.9^\circ$ and $E_i = 30.7 \text{ meV}$ plotted on a logarithmic scale. The momentum transfer ΔK ranges from 0.1 \AA^{-1} for the multiphonon peak center to 1.4 \AA^{-1} for the diffuse elastic peak.

$\theta_i = 39.9^\circ$, where the RW and LR peaks are nearly equal, and in Fig. 17 for $\theta_i = 31.9^\circ$, where the LR peak is more intense than the RW peak. At $\theta = 31.9^\circ$, it was not possible to separate the mode 2 contribution from the multiphonon background. Therefore for the data collected at $\theta_i = 31.9^\circ$, we attributed the broad background intensity completely to the multiphonon contribution.

In both Figs. 16 and 17, the multiphonon intensity already dominates all the other contributions at $T_s = 100 \text{ K}$. As shown in Fig. 11, it increases almost linearly with temperature. This behavior is described very well by the theory presented in Sec. VI. The single phonon intensities first increase with temperature up to about $T_s \approx 350 \text{ K}$ and then decrease at very high temperatures. The theory in Sec. VI B predicts a temperature dependence which varies as

$$n(\mathbf{Q}, \nu) e^{-2W} \propto T e^{-\alpha T}, \quad (1)$$

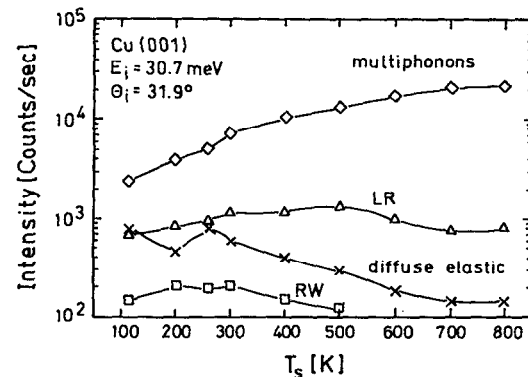


FIG. 17. Measured dependence on the surface temperature along the $\langle 100 \rangle$ azimuth of RW (\square), LR (\triangle), multiphonons (\diamond), and diffuse elastic scattering (\times) for $\theta_i = 31.9^\circ$, and $E_i = 30.7 \text{ meV}$ plotted on a logarithmic scale. The momentum transfer ΔK ranges from 0.2 \AA^{-1} for the multiphonon peak center to 2.8 \AA^{-1} for the diffuse elastic peak.

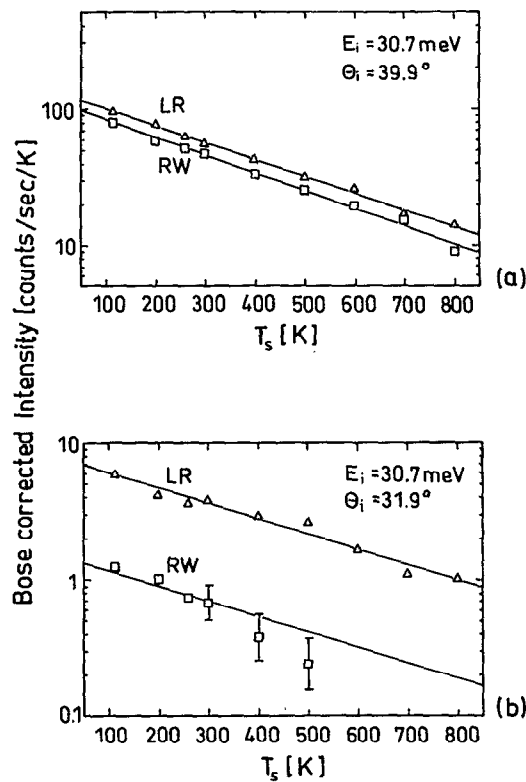


FIG. 18. Measured surface temperature dependence, corrected for the Bose factor, of the RW (\square) and LR (Δ) at $E_i=30.7$ meV. The lines are the best-fit calculations with Eq. (1) for (a) $\theta_i=39.9^\circ$, $\theta_D=267$ K, and parallel momenta $\Delta K=0.58 \text{ \AA}^{-1}$ for the RW, and $\Delta K=0.44 \text{ \AA}^{-1}$ for the LR. (b) $\theta_i=31.9^\circ$, $\theta_D=265$ K, and parallel momenta $\Delta K=1.05 \text{ \AA}^{-1}$ for the RW, and $\Delta K=0.78 \text{ \AA}^{-1}$ for the LR.

where $n(\mathbf{Q}, \nu)$ is the Bose occupation number and the standard definition of the Debye–Waller exponent in terms of the Debye temperature Θ_D is^{48(b)}

$$2W = \frac{3\hbar^2(\Delta k)^2 T}{M_{\text{Cu}} k_B \Theta_D^2}, \quad (2)$$

where M_{Cu} is the crystal atom mass. Thus by plotting the intensity divided by the temperature on a logarithmic scale vs temperature, we can correct for the Bose factor. Such Bose corrected intensities should yield a straight line, and this behavior is shown clearly in Fig. 18. Figure 18(a) is for $E_i=30.7$ meV and $\theta_i=39.9^\circ$, which corresponds to a parallel momentum transfer of $\Delta K=0.58 \text{ \AA}^{-1}$ for the RW and $\Delta K=0.44 \text{ \AA}^{-1}$ for the LR. The Debye temperature obtained via Eq. (1) for the measurements at $\theta_i=39.9^\circ$ is $\Theta_D=267$ K for both the RW and the LR. This value is somewhat larger than the Debye temperature of $\Theta_D=230$ K reported by Lapujoulade,⁴⁹ which was obtained from specular attenuation measurements on close packed Cu surfaces. Figure 18(b) shows a similar Debye–Waller plot taken at the same energy, but at $\theta_i=31.9^\circ$, where the LR peak is much larger than the RW peak. Essentially, the same value of Θ_D as obtained above provides an excellent fit of the LR peak ($\Theta_D=265$ K) and is consistent with the RW data within the experimental errors.

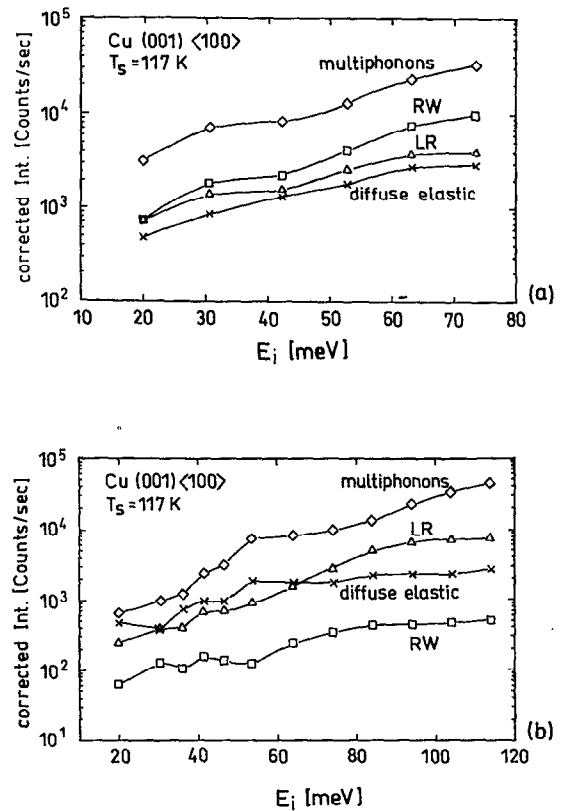


FIG. 19. Measured dependence of the corrected experimental peak intensities on incident energy. The various components are labeled as follows: diffuse elastic (\times); Rayleigh mode (\square); longitudinal resonance (Δ); and multiphonon (\diamond). The measurements were taken with all scan curves intersecting at a single point on the dispersion curve of the RW, so that there are small differences in ΔK for the other modes. (a) Data taken from the spectra shown in Fig. 8, for conditions for which the RW intensity is larger than the LR intensity along the scan curves; (b) data taken from the spectra shown in Fig. 9, for conditions for which the LR is the dominant single phonon intensity along the scan curves.

D. Energy dependence

The dependence of the corrected scattered intensities on incident energy is shown in Fig. 19 for two situations in which the parallel momentum, and hence the frequency, of the Rayleigh mode are kept constant. Some of the raw data have already been presented in Figs. 8 and 9. Since the conditions were chosen so that the scan curves pass through the same point on the RW dispersion curve, the corresponding values of ΔK for the diffuse elastic peak are slightly decreasing with E_i and slightly increasing for the LR mode. The data in Fig. 19(a) for a fixed RW parallel wave vector of $\Delta K=0.56 \text{ \AA}^{-1}$ were chosen to illustrate the behavior for a case in which the RW mode intensity is larger than the LR for all scan curves. The data in Fig. 19(b) which are for the LR wave vector $\Delta K=0.78 \text{ \AA}^{-1}$ is a case in which the LR is the dominant single phonon inelastic intensity for all scan curves. The mode 2 is not shown since it disappeared quickly with increasing energy. All of the other inelastic intensities, including the multiphonon part, increase with incident energy. Perhaps surprisingly, a similar increase is also observed for the diffuse elastic peak. This effect is in fact not due to

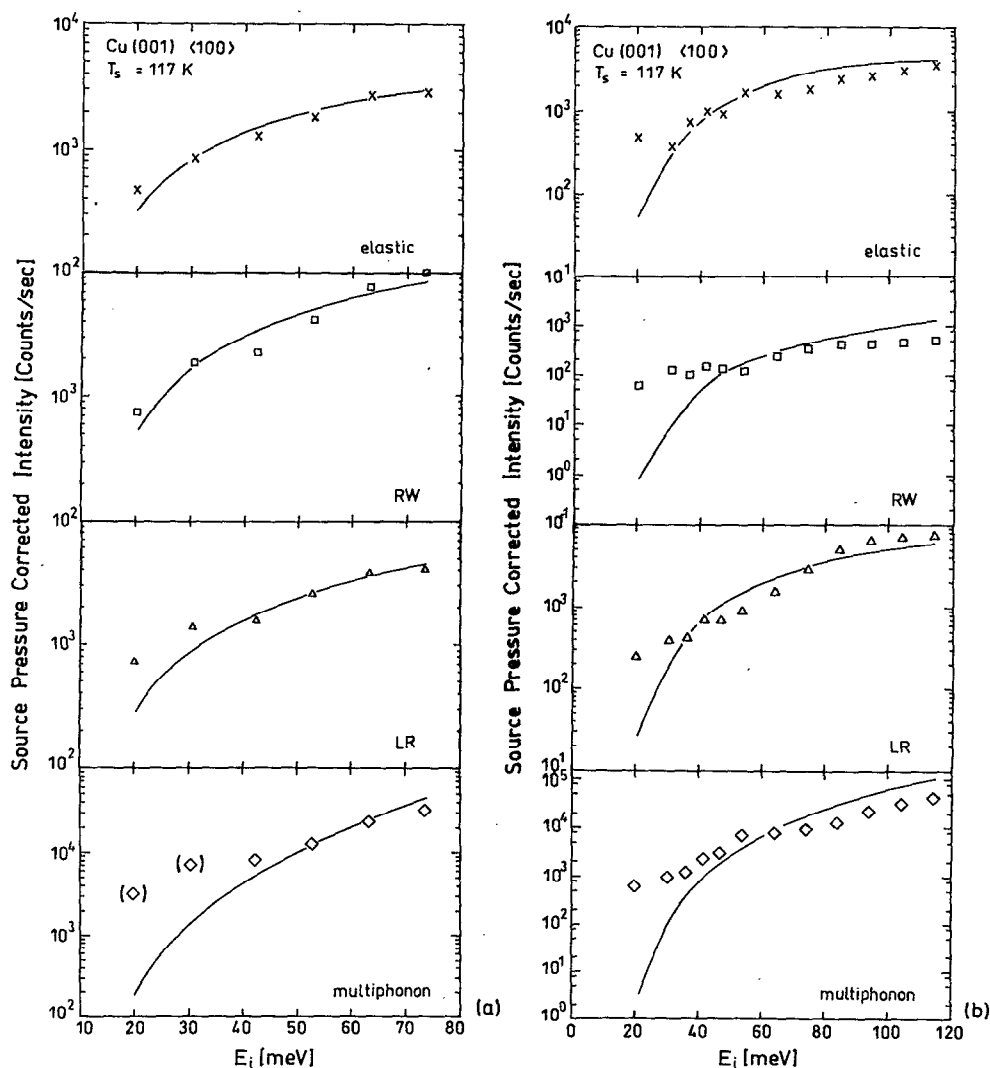


FIG. 20. A comparison of theoretical calculations with the measured incident energy dependence of the diffuse elastic, single phonon, and multiphonon scattered intensities. The symbols used for the data points are the same as used in Fig. 19. (a) RW dominant case ($\Delta k = 0.81 \text{ \AA}^{-1}$); (b) LR dominant case ($\Delta k = 0.81 \text{ \AA}^{-1}$).

the change in energy, but as explained below, comes about because of the changes of parallel momentum which is explained in the next paragraph.

Figure 20 shows the comparison with theory of each of the experimental intensities of Fig. 19. For both the RW dominant and the LR dominant cases, the calculations describe the general increase in intensity with incident energy rather well except for the very lowest energies, where the theory predicts intensities which are too small. Numerical calculations of the multiphonon behavior based on the theory, outlined in Sec. VI below, also show that the total multiphonon background contribution increases with incident energy in a manner closely matching that exhibited by the data. The parameters used for the multiphonon form factor are $\beta = 3 \text{ \AA}^{-1}$ and $Q_c = 1 \text{ \AA}^{-1}$. The calculations appear to underestimate the multiphonon contributions at energies below 40 meV. There, however, the experimental intensities may be somewhat too large since it is difficult to separate the

small multiphonon from the bulk single phonon contribution.

In agreement with the experiments, the diffuse elastic peak is also predicted to increase rather rapidly with incident energy as is shown in Fig. 19. This behavior results from the decrease in the values of ΔK corresponding to the elastic peak as E_i increases. Consequently, the strong decrease in the Debye-Waller factor is completely overcome by the sharp increase in the diffuse elastic cross section of the surface defects with decreasing ΔK shown in Fig. 15. The theoretical diffuse elastic intensities shown in Fig. 20 are calculated from an elastic transition rate, which is essentially the product of the Debye-Waller factor and the form factor, with the form factor being the same $1/\Delta K^3$ envelope as used in the calculations for Fig. 15. It is indeed gratifying that the same general and rather simple model of the scattering process shown in Fig. 20 is able to explain the general trends of the energy dependence of all three different types of scattered intensities (diffuse elastic, single phonon, and mul-

tiphonon). This would seem to indicate that the essential physics of the scattering interaction is reasonably well described by the theoretical model which is discussed next.

VI. THEORY

A. Single phonon scattering

The theory for the quantum limit of the inelastic scattering of atomic projectiles from surfaces dates back to Jackson and Mott,^{50,51} and Lennard-Jones and Devonshire⁵²⁻⁵⁴ in the early 1930s. They were stimulated by measurements of Roberts⁵⁵ of the rare gas accommodation coefficients reported in 1930 and by the experiments on the surface scattering of thermal energy helium beams published at about the same time by Stern and co-workers.⁵⁶⁻⁵⁸ Much later the distorted wave Born approximation was introduced^{59,60} in order to consider the use of helium or other rare gas atoms as scattering probes for directly measuring surface phonons. More recently, higher order quantum exchanges have been included in the perturbation series.^{61,62} In the distorted wave Born approximation, the combined system of surface plus incoming projectile beam is described by a Hamiltonian⁵⁹

$$H = H_c + H_p + V, \quad (3)$$

where H_c is the unperturbed Hamiltonian of the surface, H_p is the free particle Hamiltonian of the projectile atom, and V is the interaction coupling the two. The interaction is divided into a distorting potential V^0 , which usually includes only elastic interactions, and a remainder V^1 according to

$$V = V^0 + V^1. \quad (4)$$

This division is made by expanding V in a Taylor series in terms of the displacement variables u of the crystal atoms at the surface. V^0 is usually chosen to be the zeroth order term in the expansion, and for single phonon scattering, it is adequate to approximate V^1 by the first order term. The transition rate for scattering of an incident projectile atom of momentum $\hbar k_i = \hbar(\mathbf{K}_i, k_{iz})$ into a final state of momentum $\hbar k_f$ is given by the generalized Fermi golden rule

$$w(\mathbf{k}_f, \mathbf{k}_i) = \frac{2\pi}{\hbar} \left\langle \left\langle \sum_{\{n_f\}} |T_{fi}|^2 \delta(\mathcal{E}_f - \mathcal{E}_i) \right\rangle \right\rangle, \quad (5)$$

where \mathcal{E}_f or \mathcal{E}_i is the total energy of the system in the final or initial state, respectively. For the transition matrix, we use the Born approximation $T_{fi} \approx V_{fi}^1$ with the matrix element of V^1 taken with respect to eigenstates of the distorting potential V^0 . Since neither the initial nor final state of the crystal is in fact measured, the transition rate is summed over all final vibrational states $\{n_f\}$ and averaged over initial states as denoted by $\langle\langle \rangle\rangle$.

The differential reflection coefficient, or number of scattered particles detected per unit final solid angle and per unit final energy $d^3R/dE_f d\Omega_f$ is proportional to the transition rate. It is obtained from Eq. (5) by dividing by the incident flux and multiplying by the appropriate final density of states in phase space for the particular experimental configuration. The thermal average and many of the summations in Eq. (5) are straightforward and the general result for the differential reflection coefficient can be put in the form⁶³

$$\begin{aligned} \frac{d^3R}{dE_f d\Omega_f} &= \frac{1}{2\pi} \int d^2Q \frac{k_f}{k_{iz}} \sum_{\nu} |\langle f | \mathbf{e}(\mathbf{Q}, \nu) \cdot \nabla_u V | i \rangle|^2 \\ &\times \frac{\hbar}{M\omega(\mathbf{Q}, \nu)} n(\mathbf{Q}, \nu) e^{-2W} \delta(\mathbf{K}_f - \mathbf{K}_i - \mathbf{Q}) \\ &\times \delta[E_f - E_i - \hbar\omega(\mathbf{Q}, \nu)]. \end{aligned} \quad (6)$$

This expression is for a crystal consisting of like atoms of mass M . $\mathbf{e}(\mathbf{Q}, \nu)$ is the phonon polarization vector of the mode with parallel momentum $\hbar\mathbf{Q}$, index ν , and frequency $\omega(\mathbf{Q}, \nu)$, which is obtained from a lattice dynamical calculation. $n(\mathbf{Q}, \nu)$ is the corresponding Bose-Einstein phonon occupation number.

The Debye-Waller factor $\exp(-2W)$ in Eq. (6) does not arise naturally from the distorted wave Born approximation, but must rather be viewed as arising from an approximate resummation of all higher order terms in the perturbation series.^{47,63} The simplest expression for the Debye-Waller factor, and one which is adequate for the experimental analysis here, is the classic expression in which the exponent is given by the displacement correlation function of a single crystal atom

$$2W = \langle\langle |\mathbf{k} \cdot \mathbf{u}_l(t)|^2 \rangle\rangle, \quad (7)$$

where $\mathbf{k} = \mathbf{k}_f - \mathbf{k}_i$ and $2W$ is independent of both time t and lattice position l . Equation (2) above is obtained from Eq. (7) with the use of a Debye frequency distribution function.

Most treatments up to now have approximated the scattering potential by a sum of effective two-body potentials between the He atom and each surface atom. The repulsive part of the atomic pair potentials is usually described by the Born-Mayer form $v_0 \exp(-\beta r)$, where β is the range parameter and r is the distance from the core center. The sum of such potentials results in a He-surface potential whose repulsive part is an overall exponential repulsion with respect to distance z away from the surface $v_0 \exp(-\beta z)$ multiplied by a more complicated function describing the potential corrugation parallel to the surface and the vibrations. Both the softness of the exponential repulsion and the fact that the He projectile interacts with more than one surface atom simultaneously reduces the response to short wavelength phonons of the parallel wave vector $Q > Q_c$. A reasonable approximation of this effect leads to a cut-off factor $\exp(-Q^2/2Q_c^2)$, and in this approximation, the matrix elements appearing in Eq. (6) are given by⁶⁴

$$\begin{aligned} \langle f | \mathbf{e}(\mathbf{Q}, \nu) \cdot \nabla_u V | i \rangle &= v_0 \langle k_{fz} | e^{-\beta z} | k_{iz} \rangle \\ &\times e^{-Q^2/2Q_c^2} [i\mathbf{Q} \cdot \mathbf{e}(\mathbf{Q}, \nu) + \beta e_z(\mathbf{Q}, \nu)]. \end{aligned} \quad (8)$$

As discussed in the Introduction, the helium atoms are elastically scattered by the oscillations of the surface electron density in response to the vibrations of the underlying nuclei. The electron density, and hence the scattering potential, is thus a complicated function of the core positions. In the recently introduced pseudocharge model,^{5,6} the interaction potential is obtained by assuming a direct proportionality of the electron density $V(\mathbf{r}) = A \delta\rho(\mathbf{r})$, where A is a proportionality

factor. Additional terms are added to the matrix element of Eq. (8), which are of the same form as (8), but with renormalized polarization vectors, to account for the dynamical coupling of the He atoms to the pseudocharges.

The information on the dynamics of the phonons is contained in the polarization vectors $e_{\alpha}^{\kappa}(\mathbf{Q}, \nu)$, where the α 's are the Cartesian coordinates. For a lattice consisting of unit cells with a basis of atoms of mass M_{κ} denoted by the symbol κ , the phonon spectral density is defined by

$$\rho_{\kappa, \kappa'}^{\alpha, \alpha'}(\mathbf{Q}, \omega) = \sum_{\nu} \frac{\hbar}{2S_{\text{u.c.}} \omega(\mathbf{Q}, \nu) \sqrt{M_{\kappa} M_{\kappa'}}} \times e_{\alpha}^{\kappa}(\mathbf{Q}, \nu) e_{\alpha'}^{\kappa'}(\mathbf{Q}, \nu) \delta[\omega - \omega(\mathbf{Q}, \nu)], \quad (9)$$

where $S_{\text{u.c.}}$ is the area of the surface unit cell. Then, upon defining a new vector $\mathbf{q} = (i\mathbf{Q}, \beta)$ Eq. (6), expressed as a transition rate as in Eq. (5), is reduced to a very simple form, which we write here for scattering from a single surface layer of Bravais unit cells⁴⁷

$$w(\mathbf{k}_f, \mathbf{k}_i) = \frac{2\pi S_{\text{u.c.}}}{\hbar} |v_{\beta}|^2 e^{-2W} \sum_{\alpha\alpha'}^3 q_{\alpha} q_{\alpha'}^* [\rho^{\alpha, \alpha'}(-\mathbf{Q}, \omega) \times [n(\mathbf{Q}, \omega) + 1] + \rho^{\alpha, \alpha'}(\mathbf{Q}, \omega) n(\mathbf{Q}, \omega)]. \quad (10)$$

The two terms in the brackets describe phonon annihilation and creation, respectively, and each term is the product of the transition matrix elements of the form factor $|v_{\beta}|^2$, a Debye–Waller factor, a Bose occupation factor, and the phonon spectral density. The latter will be looked upon as an effective structure factor. Equation (10) shows that in this simple interpretation, the He scattering intensities from single phonons are directly proportional to the spectral density. The more exact case of Eq. (6) shows that the true situation is a convolution of the spectral density with the matrix elements of the potential. However, Eq. (10) is a reasonable and useful approximation, and is the expression that we have used in Sec. IV for the interpretation of the intensities of both the Rayleigh mode and the longitudinal resonance. We realize that this theory can only give effective coupling parameters for the LR phonons since these involve a different excitation mechanism involving pseudocharges.^{5,9}

The form factor we use with Eq. (10) is given by

$$|v_{\beta}|^2 = v_0^2 |\langle k_{fz} | e^{-\beta z} | k_{iz} \rangle|^2 e^{-Q^2/Q_c^2}. \quad (11)$$

For an exponential repulsive potential $v_0 e^{-\beta z}$, the matrix elements are given by the Mott–Jackson formula.⁵⁰ Corresponding to the relationship of the potential to the charge density, this translates into a dependence on the change in charge density with distance from the surface. Since the distorted wave Born approximation (DWBA) theory of Eq. (10) is based on a phenomenological potential, assumed proportional to the surface charge density, it should be equally applicable to a description of the RW or LR regardless of the fact that the underlying vibrational motion of the ion cores is expected to be quite different for the two different modes. By applying the DWBA theory^{59,64} of Eq. (10) to the data, we can, in principle, obtain from the matrix element for perpen-

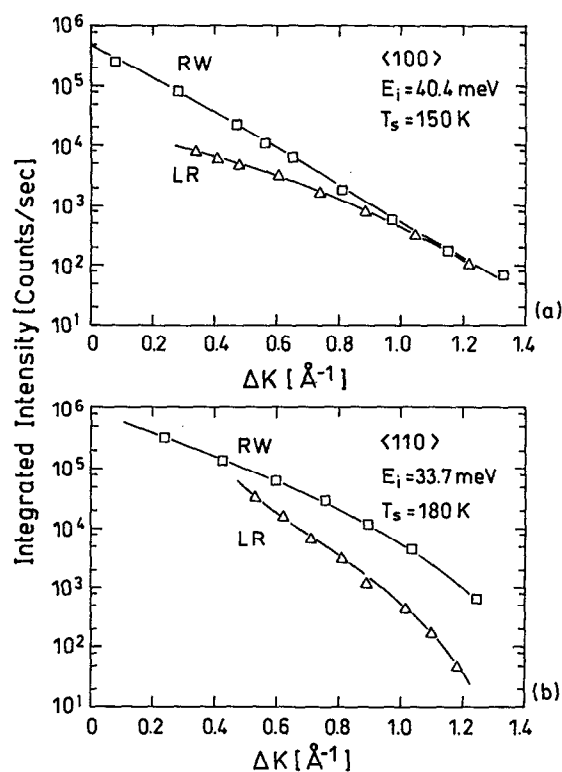


FIG. 21. Momentum transfer dependence of the intensity of the RW and the LR peaks (a) along the $\langle 100 \rangle$ direction and (b) along the $\langle 110 \rangle$ direction. The solid lines are from the theory of Eq. (10), calculated with the parameters shown in Table II.

dicular motion the range parameter of the repulsive part of the potential β and a cut-off factor Q_c . Clearly, from Fig. 15 or the more detailed plots in Fig. 21, the slope of the curve for the LR is smaller than that of the RW. This difference suggests that the interactions for the two modes have different coupling potentials.

When Eq. (10) is used to fit either the RW or LR curves of Fig. 15, a unique pair of values for β and Q_c is not obtained readily. Instead, we find that a large range of parameter pairs fits the data equally well within the experimental error, contrary to the case for other metal surfaces such as Ag(111)⁶⁴ or Rh(111),⁶⁵ where the same fitting procedure yielded a very narrow range of values. The corresponding parameter curves of equal fit quality are shown in Fig. 22. However, the parameters β and Q_c are also related to the classical turning point z_t above the surface via $\beta = z_t Q_c^2$.^{64,66} Recently it has been possible to measure z_t directly for the Cu(001) surface.⁷⁵ The measured value $z_t = 2.88 \text{ \AA}$ allows for a unique determination of both parameters (see Fig. 22). The resulting potential parameters are collected in Table II, where they are compared with determinations for other surfaces. A comparison of the potential parameters along the different directions shows along $\langle 100 \rangle$ a much stiffer potential for the LR ($\beta = 5.0 \text{ \AA}^{-1}$) than for the RW ($\beta = 3.0 \text{ \AA}^{-1}$). This behavior is expected from the observed strong LR excitation along this direction. Along the $\langle 110 \rangle$ direction, the comparatively smaller LR scattering intensity corresponds to

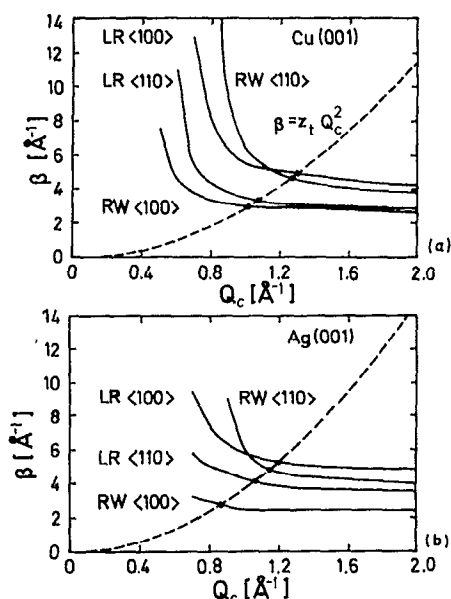


FIG. 22. Curves of best-fit values for the potential parameters β and Q_c of Eq. (10) for (a) Cu(001) and (b) Ag(001). The dashed curves represent parameter combinations corresponding to classical turning points of (a) $z_t = 2.88 \text{ \AA}$ for Cu(001) (Ref. 75) and (b) $z_t = 3.66 \text{ \AA}$ for Ag(001) (Ref. 76).

a small steepness for the LR ($\beta = 3.35 \text{ \AA}^{-1}$) when compared with the RW value of ($\beta = 4.67 \text{ \AA}^{-1}$).

B. Multiple phonon transfers

From Eq. (10), it is clear that the interesting physics in the single phonon intensities is contained in the transition matrix element of the form factor, which provides information on the He-surface interaction, and in the phonon spectral density which describes the surface lattice dynamics. However, a substantial diffuse inelastic background, which is always present in the experimental time-of-flight intensity curves, must be still accounted for. This diffuse intensity comes from three major sources, excitations of the continuous distribution of bulk single phonon modes, incoherent inelastic contributions arising from defects and imperfections on the surface, and coherent multiphonon transfers. For the interpretation of the experiments, the background also needs to be understood so that it can be properly subtracted from the TOF spectra in order to extract the single phonon contributions. Since the surfaces used in the present experiments are very clean and well ordered as indicated by the small incoherent elastic peaks, we can safely assume that the background is due almost entirely to single bulk phonons and multiphonon transfers.

Several approaches to the multiphonon quantum transfer of energy at surfaces have been proposed.^{42,47,62,63,77,78} An approach which has been shown to be quite adequate for describing the multiphonon background in atom-surface scattering is derived from a combination of the trajectory approximation and the quick scattering limit.^{47,79} This can be embodied in the following simple form of the transition matrix:

TABLE II. Potential parameters β , Q_c , and effective Debye temperatures θ_D for different metal surfaces.

	Direction	Mode	$\beta(\text{\AA}^{-1})$	$Q_c(\text{\AA}^{-1})$	$\theta_D(\text{K})$
Cu(001)	$\langle 100 \rangle$	RW	3.0 ^a	1.0 ^a	267 ^a
Cu(001)	$\langle 100 \rangle$	LR	5.0 ^a	1.32 ^a	267 ^a
Cu(001)	$\langle 110 \rangle$	RW	4.67 ^a	1.28 ^a	267 ^a
Cu(001)	$\langle 110 \rangle$	LR	3.35 ^a	1.08 ^a	267 ^a
Cu(001)	$\langle 100 \rangle$	RW	2.1 ^d	0.95 ^d	230 ^c
					280 ^b
Ag(001)	$\langle 100 \rangle$	RW	2.77 ^b	0.87 ^b	253 ⁱ
Ag(001)	$\langle 100 \rangle$	LR	5.30 ^b	1.20 ^b	253 ⁱ
Ag(001)	$\langle 110 \rangle$	RW	4.85 ^b	1.15 ^b	253 ⁱ
Ag(001)	$\langle 110 \rangle$	LR	4.12 ^b	1.06 ^b	253 ⁱ
Ag(111)	$\langle 11\bar{2} \rangle, \langle 110 \rangle$	RW	4.0 ^c	0.74 ^c	145 ^j
Au(111)	$\langle 11\bar{2} \rangle, \langle 110 \rangle$	RW	2.10 ^g	0.74 ^g	...
Rh(111)	$\langle 11\bar{2} \rangle, \langle 110 \rangle$	RW	3.15 ^f	0.82 ^f	255 ^k
Pt(111)	$\langle 11\bar{2} \rangle, \langle 110 \rangle$	RW	...	0.57 ^m	111 ^l
Ni(110)	$\langle 100 \rangle$	RW	2.92 ⁿ	0.84 ⁿ	595 ⁱ
Al(111)	$\langle 11\bar{2} \rangle, \langle 110 \rangle$	RW	4.0 ^o	0.92 ^o	...

^aPresent work.

^bReference 10.

^cReference 49.

^dReference 61.

^eReference 64.

^fReference 65.

^gReference 66.

^hReference 67.

ⁱReference 68.

^jReference 69.

^kReference 70.

^lReference 71.

^mReference 72.

ⁿReference 73.

^oReference 74.

$$T_{\mathbf{k}_f, \mathbf{k}_i} = \sum_l \tau_{fi}^l \exp[-i\mathbf{k} \cdot (\mathbf{r}_l + \mathbf{u}_l)], \quad (12)$$

where \mathbf{r}_l is the position of the l th unit cell and \mathbf{u}_l is its displacement, again assuming a Bravais surface lattice. In the quick collision limit, the time that the projectile remains near the surface is short compared with relevant vibrational periods. Although this approximation is not adequate for higher energy single phonon transfers, it is a reasonable approximation for the multiphonon background since it is dominated by small frequency and long wavelength modes.^{80,81} The quick scattering assumption is equivalent to assuming that the scattering amplitude τ_{fi}^l in Eq. (12) is independent of the vibrational amplitudes \mathbf{u} . The trajectory approximation implies that the projectile follows a single classically allowed path in going from the initial state of momentum $\hbar\mathbf{k}_i$ to the final state $\hbar\mathbf{k}_f$. In the quick collision limit, the choice of path becomes unimportant and depends only on the limiting end points of the path, or on the total transferred momentum $\hbar\mathbf{k}$.

When the transition matrix of Eq. (12) is inserted into the golden rule expression of Eq. (5), the resulting transition rate can be expressed in terms of the displacement correlation function $\langle\langle \mathbf{k} \cdot \mathbf{u}_l(t) \mathbf{k} \cdot \mathbf{u}_{l'}(t') \rangle\rangle$ as follows:⁴⁷

$$w(\mathbf{k}_f, \mathbf{k}_i) = \frac{1}{\hbar^2} \int_{-\infty}^{+\infty} dt e^{-\Delta E t / \hbar} \sum_l |\tau_{fi}^l|^2 e^{-2W} \times \exp[\langle\langle \mathbf{k} \cdot \mathbf{u}_0(0) \mathbf{k} \cdot \mathbf{u}_l(t) \rangle\rangle]. \quad (13)$$

In general, the summation over surface lattice sites in Eq. (13) can give rise to structure in the scattered intensity analogous to Kikkuchi lines in electron scattering. However, at the high energies and temperatures used in these experiments, such effects are small and of no consequence and each unit

cell can therefore be treated as an independent scatterer. Thus the final expression for the multiphonon differential reflection coefficient reduces to

$$\frac{d^3R}{dE_f d\Omega_f} = \frac{m^2 k_f}{(2\pi)^3 \hbar^5 k_{iz}} |\tau_{fi}|^2 e^{-2W} \int_{-\infty}^{+\infty} dt e^{-\Delta E t/\hbar} \times \{ \exp[\langle (\mathbf{k} \cdot \mathbf{u}_0(0) \mathbf{k} \cdot \mathbf{u}_0(t)) \rangle] - 1 - \langle (\mathbf{k} \cdot \mathbf{u}_0(0) \mathbf{k} \cdot \mathbf{u}_0(t)) \rangle \}. \quad (14)$$

For the form factor $|\tau_{fi}|^2$, we use the same first order distorted wave Born approximation of Eq. (11), while for calculating the displacement correlation functions, we simplify one step further by using a Debye phonon model. The zeroth and first order terms which are subtracted from the exponentiated correlation function in Eq. (14) can be identified as the elastic peak (which is a singular δ -function contribution) and the single phonon contribution, respectively. They have been subtracted since we are only interested in the multiphonon contributions.

C. A comparison of multiphonon calculations with experiment

We elaborate here on the direct comparisons between the experimentally measured data and the calculations in order to demonstrate and justify the methods used above in Sec. IV for separating out the multiphonon contributions from those of the bulk single phonons. A more complete and detailed description of the multiphonon behavior of the He-Cu system will be presented elsewhere.⁴³ Figure 23 shows an experimental time-of-flight spectrum converted to energy transfer for an incident He beam of $E_i = 82$ meV, $\theta_i = 50.9^\circ$, and a surface temperature $T_s = 800$ K. Under these extreme multiphonon conditions, the broad peak observed in the neighborhood of $\Delta E \approx 9$ meV is nearly entirely due to multiphonon exchange; the Debye-Waller factor is so small that the single phonon RW and LR peaks that also appear in this same energy region at lower temperatures have completely disappeared. The solid curve is the calculation from Eq. (14) using a Debye temperature $\Theta_D = 280$ K and potential parameters $\beta = 3.1 \text{ \AA}^{-1}$ and $Q_c = 0.9 \text{ \AA}^{-1}$. These parameters are very close to and give a slightly better fit than the values $\beta = 3.0 \text{ \AA}^{-1}$ and $Q_c = 1.0 \text{ \AA}^{-1}$ used to fit the RW temperature and energy dependencies shown in Fig. 20 above. The shape of the calculated curve, which agrees nicely with experiment in both FWHM and peak position, is nearly Gaussian which justifies the use of Gaussian curves for modeling the multiphonon contribution in the analysis of Sec. IV.

Both the FWHM and the peak position of the theoretical multiphonon intensity curve shown in Fig. 23 are rather sensitive to changes in β and Q_c . By contrast, the dependence of the multiphonon intensities on temperature and incident energy are much less sensitive to these parameters. We note that the multiphonon intensity contains contributions from the RW, LR, and the bulk modes, so we do not expect the values of β and Q_c obtained from the multiphonon intensities necessarily to be identical with those values obtained from the single phonon intensities as calculated from Eq. (9).

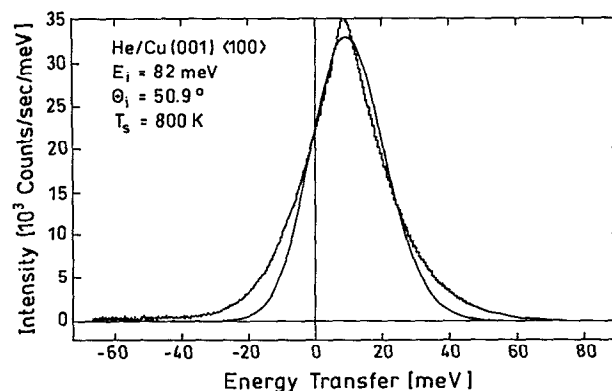


FIG. 23. The measured inelastic intensity as a function of energy transfer for $E_i = 82$ meV and $\theta_i = 50.9^\circ$ and a surface temperature $T = 800$ K under extreme multiphonon excitation conditions. The solid curve is a calculation based on Eq. (14) with a Debye temperature $\Theta_D = 280$ K and potential parameters $\beta = 3.1 \text{ \AA}^{-1}$ and $Q_c = 0.9 \text{ \AA}^{-1}$.

In Fig. 11, the temperature dependence of the area under the multiphonon peak is plotted as a function of temperature for two different incident angles $\theta_i = 39.9^\circ$ and 31.9° , both with energy $E_i = 31$ meV. The experimental points were obtained by a Gaussian fit to the data as discussed in Sec. IV and the theoretical curve was calculated from Eq. (14) with $\Theta_D = 280$ K, with the calculated curve normalized to the experimental point at $T_s = 600$ K. The calculated curve is rather weakly dependent on the choice of Θ_D , with larger values of Θ_D giving a larger slope and smaller values giving a somewhat smaller slope. The results for the calculated slopes in Fig. 11 are quite independent of the potential parameters over a large range of values. For the actual curves presented, we used $\beta = 3.0 \text{ \AA}^{-1}$ and $Q_c = 1.0 \text{ \AA}^{-1}$, the same values obtained from the analysis of the RW single phonon peak in Fig. 21.

We have also compared theory with experiment for the position and FWHM of the multiphonon peak as a function of temperature and for the peak position as a function of incident angle.⁴³ The theory predicts FWHMs which agree quantitatively with experiment as shown by the example in Fig. 23 and over a wide range of temperature as shown in Fig. 12. The measured multiphonon peak position shows no shift, within the experimental resolution of 0.6 meV, as a function of surface temperature, in agreement with the theory which also predicts negligible shift.

As a function of incident angle, the dispersion curve of the multiphonon peak is observed to have a behavior much the same as that of the single phonon RW and LR peaks; with increasing ΔK , the multiphonon peak moves monotonically from $\Delta E \approx 0$ to larger positive values of ΔE , while for negative ΔK , the multiphonon peak appears at negative energy exchange.⁴² The measured and calculated behaviors of the peak position with incident angle are very similar.

VII. DISCUSSION

In this paper, we have reported extensive measurements of the helium atom surface phonon intensities in inelastic helium scattering from Cu(001) in both the $\langle 100 \rangle$ and $\langle 110 \rangle$

symmetry directions. The measured dispersion curves confirm the previous results,⁹ which exhibited, along with the Rayleigh mode, a clearly visible longitudinal resonance. In the $\langle 100 \rangle$ direction, the LR is very strong, and for a range of scan curves involving the larger values of ΔK close to the Brillouin zone boundary, it appears more intense than the RW mode. In fact, the LR peak in the intensity can be measured well into the second Brillouin zone. However, in the $\langle 110 \rangle$ direction, the LR is much weaker in intensity than the RW mode.

We have investigated carefully the dependence of the inelastic intensities as a function of incident energy, parallel momentum transfer, and surface temperature. In order to better distinguish and isolate the diffuse elastic and the single phonon RW and LR from the diffuse inelastic background due to the single bulk phonons and due to multiphonon transfers, we have developed a novel decomposition technique for analyzing the experimental data. The first step of this process is to extract each of these distinct components from the total inelastic time-of-flight intensities using Gaussian functions. The use of Gaussian curves for these contributions is justified because their width and shape are dominated by the resolving power of the experimental apparatus which is expected to produce Gaussian shapes in the energy transfer.³⁹

The contributions of the multiphonons and the bulk single phonons excited at the surface are not so straightforward to identify because both form a broad continuum in the energy transfer. However, we are able to accomplish the separation by making use of the significantly different surface temperature dependence of these two contributions, and by the fact that the multiphonon contribution dominates the inelastic intensity at high temperatures and is predicted to have a nearly Gaussian shape. Thus, in the high temperature range, we can identify the multiphonon component by a direct comparison with theoretical predictions, and then the theory gives dependable predictions of the multiphonon part at lower surface temperatures. The bulk single phonon contributions become important at low temperatures and appear in the same range of energy exchange as the multiphonon contribution. They could be extracted by subtracting off the Gaussian shaped multiphonon background predicted by the theory. Further confirmation of the correct identification of the bulk single phonon contribution is provided by checking its temperature dependence, and we find that its behavior is described well by the product of a Bose occupation function and a Debye-Waller factor, as expected for a single phonon transfer process. After isolating each of the individual components making up the inelastic TOF spectra, we have analyzed their behaviors as a function of the variation of the incident beam and surface parameters with the aid of an inelastic scattering theory.⁴⁷

The temperature dependence of the diffuse elastic peak, all single phonon peaks (including the bulk single phonon part), and the multiphonon contribution were measured over a temperature range of $100 < T < 1000$ K. In the lower part of this temperature range, the single phonon peaks were found to increase with temperature, while at higher temperature, they began to decrease, in good agreement with the Debye-Waller behavior predicted by Eq. (1). The mul-

tiphonon contribution, on the other hand, was found to be a monotonically increasing function over this entire temperature range, except for the case of very high incident energies. The temperature dependence of almost all the peaks, including the incoherent elastic peak, agreed well with the theory within the experimental error with a Debye temperature which was approximately 270 K. [The bulk Debye temperature of Cu is generally accepted to be about 320 K (Ref. 82).]

The intensities of all contributions (incoherent elastic, single phonon, and multiphonon) were found to increase with incident collision energy, in general agreement with theory. The surprisingly good prediction of the theory for general trends of all of the measured intensities as a function of incident energy is a strong confirmation that the essential features of the physics of the scattering interaction are contained in the theoretical model used throughout this work.

The behavior of the inelastic intensities with parallel momentum is very interesting. The diffuse elastic peak decreases strongly with increasing parallel wave vector ΔK from its maximum near the specular peak at $\Delta K = 0$ with a $1/\Delta K^3$ behavior expected from the envelope of hard core Fraunhofer scattering by a collection of point defects.

Several significant new results come from the analysis of the ΔK dependence of the single phonon peaks. As a function of ΔK , both the RW and LR intensities decay rapidly, with a pronounced azimuthal dependence of the decay rate. We find that the simple and widely accepted form factor for single phonon transfers,⁶³ which is the product of a cut-off factor and a Mott-Jackson type matrix element of Eq. (11), works well for fitting the data, but does not produce a well-defined set of parameters. However, the fit can be made unique by taking into account the recently measured value of the turning point of the He atoms above the Cu surface. The LR intensity along the $\langle 110 \rangle$ direction is described by an effective scattering potential comparable to that of the RW mode. However, along the $\langle 100 \rangle$ direction, the observed, comparatively slow decay of the LR intensity is described by a steeper potential with a large value of β . The physical origin of this slow intensity decay has been attributed to the comparatively large amplitude of the LR vibration along $\langle 100 \rangle$ due to the absence of nearest neighbors in this direction.⁹ This observation supports the idea that the primarily longitudinal polarized vibrations of the LR couple strongly to the conduction electrons and cause the electron density near the surface to have a vertical vibrational corrugation.

In closing, we would like to express our hope that this extensive data base will stimulate the further development of dynamical theories of surface phonon excitation by atom impact.

ACKNOWLEDGMENTS

We would like to thank Paolo Ruggerone and Luo Ninsheng for helpful discussions on theoretical aspects and Gregor Witte for discussions and help with the data analysis. One of us (J.R.M.) was supported by the NSF under Grant No. DMR 9114015.

- ¹R. B. Doak, U. Harten, and J. P. Toennies, *Phys. Rev. Lett.* **51**, 578 (1983).
- ²U. Harten, J. P. Toennies, and Ch. Wöll, *Faraday Discuss. Chem. Soc.* **80**, 137 (1985).
- ³J. P. Toennies, *Springer Series in Surface Sciences*, edited by F. de Wette (Springer, Heidelberg, 1988), Vol. 14, p. 248.
- ⁴G. Benedek and J. P. Toennies, *Surf. Sci. Rep.* (to be published).
- ⁵C. Kaden, P. Ruggerone, J. P. Toennies, G. Zhang, and G. Benedek, *Phys. Rev. B* **46**, 13509 (1992).
- ⁶C. Kaden, P. Ruggerone, J. P. Toennies, and G. Benedek, *Nuovo Cimento D* **14**, 627 (1992).
- ⁷B. F. Mason and B. R. Williams, *Phys. Rev. Lett.* **46**, 1138 (1981).
- ⁸J. Ellis, E. M. McCash, and W. Allison, *J. Electron. Spectrosc.* **54/55**, 325 (1990).
- ⁹G. Benedek, J. Ellis, N. S. Luo, A. Reichmuth, P. Ruggerone, and J. P. Toennies, *Phys. Rev. B* **48**, 4917 (1993).
- ¹⁰N. Bunjes, P. Ruggerone, J. P. Toennies, and G. Witte (to be published).
- ¹¹V. Bortolani, D. Cvetko, F. Floreano, A. Franchini, A. Lausi, A. Morgante, M. Peloi, G. Santoro, F. Tommasini, T. Zambelli, and A. F. Altmann, *J. Electron. Spectrosc. Relat. Phenom.* **64**, 671 (1993).
- ¹²M. Wuttig, R. Franchy, and H. Ibach, *Solid State Commun.* **57**, 445 (1986).
- ¹³M. Wuttig, R. Franchy, and H. Ibach, *Z. Phys. B Condensed Matter* **65**, 71 (1986).
- ¹⁴L. L. Kesmodel, M. L. Xu, and S. Y. Tong, *Phys. Rev. B* **34**, 2010 (1986).
- ¹⁵V. Bortolani, G. Santoro, U. Harten, and J. P. Toennies, *Surf. Sci.* **148**, 82 (1984).
- ¹⁶V. Bortolani, A. Franchini, G. Santoro, and F. Nizzoli, *Phys. Rev. Lett.* **52**, 429 (1984).
- ¹⁷V. Bortolani, A. Franchini, and G. Santoro, in *Electronic Structure, Dynamics and Quantum Structural Properties of Condensed Matter*, edited by J. T. Devreese and P. Van Camp (Plenum, New York, 1985), p. 401.
- ¹⁸G. Santoro, A. Franchini, V. Bortolani, U. Harten, J. P. Toennies, and Ch. Wöll, *Surf. Sci.* **183**, 180 (1987).
- ¹⁹V. Bortolani, A. Franchini, G. Santoro, J. P. Toennies, Ch. Wöll, and G. Zhang, *Phys. Rev. B* **40**, 3524 (1989).
- ²⁰M. H. Mohamed, L. L. Kesmodel, B. M. Hall, and D. L. Mills, *Phys. Rev. B* **37**, 2763 (1988).
- ²¹B. M. Hall, D. L. Mills, M. H. Mohammed, and L. L. Kesmodel, *Phys. Rev. B* **38**, 5856 (1988).
- ²²W. Cochran, *Proc. R. Soc. London Ser. A* **253**, 260 (1959).
- ²³J. C. Phillips, *Phys. Rev.* **166**, 832 (1968).
- ²⁴R. M. Martin, *Phys. Rev.* **186**, 871 (1969).
- ²⁵W. Weber, *Phys. Rev. Lett.* **33**, 371 (1974).
- ²⁶W. Weber, *Phys. Rev. B* **15**, 4789 (1977).
- ²⁷C. S. Jayanthi, H. Bilz, W. Kress, and G. Benedek, *Phys. Rev. Lett.* **59**, 795 (1991).
- ²⁸Note that not all core motions parallel to the surface will necessarily give rise to vertical distortions of the surface electron density. For example, in the case of the shear horizontal mode on the Cu(001) surface, the core motions are coordinated in such a way that the distances between cores remain constant up to second order in the displacement. Thus in this case, the pseudocharges probably are also undistorted and no observable effect on the surface is expected.
- ²⁹Y. Chen, S. Y. Tong, J. Kim, L. L. Kesmodel, T. Rodach, K. P. Bohnen, and K. M. Ho, *Phys. Rev. B* **44**, 11394 (1991).
- ³⁰K. M. Ho and K. P. Bohnen, *Phys. Rev. Lett.* **56**, 934 (1986).
- ³¹K. M. Ho and K. P. Bohnen, *J. Electron. Spectrosc.* **54/55**, 229 (1990).
- ³²Y. Chen, S. Y. Tong, Jae-Sung Kim, L. L. Kesmodel, T. Rodach, K. P. Bohnen, and K. M. Ho, *Phys. Rev. B* **44**, 11394 (1991).
- ³³Y. Chen, S. Y. Tong, K. P. Bohnen, T. Rodach, and K. M. Ho, *Phys. Rev. Lett.* **70**, 603 (1993).
- ³⁴P. D. Ditlevsen and J. K. Nørskov, *J. Electron Spectrosc.* **54/55**, 237 (1990).
- ³⁵J. S. Nelson, E. C. Sowa, and M. S. Daw, *Phys. Rev. Lett.* **61**, 1977 (1988).
- ³⁶Luo Ningsheng, X. Wenlan, and S. C. Shen, *Solid State Commun.* **67**, 837 (1988).
- ³⁷J. P. Toennies, in *Springer Series in Surface Sciences*, edited by W. Kress and F. W. de Wette (Springer, Heidelberg, 1991), Vol. 21, p. 111.
- ³⁸Commercially available from Beam Dynamics, Inc., 708 East 56th Street, Minneapolis, MN 55417.
- ³⁹D. M. Smilgies and J. P. Toennies, *Rev. Sci. Instrum.* **59**, 2185 (1988).
- ⁴⁰The experimental half-width was simply calculated assuming Gaussian distributions so that $\delta = (\delta_{\text{expt}}^2 - \delta_{\text{app}}^2)^{1/2}$, where δ_{expt} is the observed and δ_{app} is the apparatus FWHM calculated from Ref. 39.
- ⁴¹Luo Ningsheng (private communication).
- ⁴²V. Celli, D. Himes, P. Tran, J. P. Toennies, Ch. Wöll, and G. Zhang, *Phys. Rev. Lett.* **66**, 3160 (1991).
- ⁴³F. Hofmann, J. P. Toennies, and J. R. Manson (to be published).
- ⁴⁴A. Franchini, V. Bortolani, G. Santoro, V. Celli, G. Eguluz, J. H. Gaspar, M. Gester, A. Lock, and J. P. Toennies, *Phys. Rev. B* **47**, 4691 (1993).
- ⁴⁵J. A. Gaspar, A. G. Eguluz, M. Gester, A. Lock, and J. P. Toennies, *Phys. Rev. Lett.* **66**, 337 (1991).
- ⁴⁶A. L. Lahee, J. R. Manson, J. P. Toennies, and Ch. Wöll, *J. Chem. Phys.* **88**, 7194 (1987).
- ⁴⁷J. R. Manson, *Phys. Rev. B* **43**, 6924 (1991).
- ⁴⁸(a) D. Eichenauer, U. Harten, J. P. Toennies, and V. Celli, *J. Chem. Phys.* **86**, 3693 (1987). (b) A. C. Levi and H. Suhl, *Surf. Sci.* **88**, 227 (1979).
- ⁴⁹J. Lapujoulade, J. Perreau, and A. Kara, *Surf. Sci.* **129**, 59 (1983); G. Armand, J. Lapujoulade, and Y. Lejay, *Proceedings of the Seventh International Vacuum Congress and the Third International Conference on Solid Surfaces of the International Union for Vacuum Science, Technique and Applications*, edited by R. Dobrozemsky, F. Rüdener, F. P. Viehböck, and A. Breth (Berger & Söhne, Vienna, 1977).
- ⁵⁰J. M. Jackson and N. F. Mott, *Proc. R. Soc. London Ser. A* **137**, 703 (1932).
- ⁵¹J. M. Jackson, *Proc. Cambridge Philos. Soc.* **28**, 136 (1932).
- ⁵²J. E. Lennard-Jones and A. F. Devonshire, *Proc. R. Soc. London Ser. A* **156**, 6 (1937); **156**, 29 (1937).
- ⁵³J. E. Lennard-Jones and A. F. Devonshire, *Proc. R. Soc. London Ser. A* **158**, 253 (1937).
- ⁵⁴A. F. Devonshire, *Proc. R. Soc. London Ser. A* **158**, 269 (1937).
- ⁵⁵J. K. Roberts, *Proc. R. Soc. London Ser. A* **129**, 146 (1930).
- ⁵⁶F. Knauer and O. Stern, *Z. Phys.* **53**, 766 (1929).
- ⁵⁷I. Estermann and O. Stern, *Z. Phys.* **61**, 95 (1930).
- ⁵⁸I. Estermann, R. Frisch, and O. Stern, *Z. Phys.* **73**, 348 (1931).
- ⁵⁹R. Manson and V. Celli, *Surf. Sci.* **24**, 495 (1971).
- ⁶⁰N. Cabrera, V. Celli, and R. Manson, *Phys. Rev. Lett.* **22**, 396 (1969).
- ⁶¹G. Armand and J. R. Manson, *Phys. Rev. B* **25**, 6195 (1982).
- ⁶²J. R. Manson and G. Armand, *Surf. Sci.* **195**, 513 (1988).
- ⁶³V. Bortolani and A. C. Levi, *Riv. Nuovo Cimento* **9**, 1 (1986).
- ⁶⁴V. Celli, G. Benedek, U. Harten, J. P. Toennies, R. B. Doak, and V. Bortolani, *Surf. Sci.* **143**, L376 (1984).
- ⁶⁵G. Witte, J. P. Toennies, and Ch. Wöll, *Surf. Sci.* (to be published).
- ⁶⁶V. Bortolani, A. Franchini, N. Garcia, F. Nizzoli, and G. Santoro, *Phys. Rev. B* **28**, 7358 (1983).
- ⁶⁷M. Foss, F. Besenbacher, C. Klink, and I. Stensgard, *Chem. Phys.* **215**, 535 (1993).
- ⁶⁸J. M. Horne, C. Yerkes, and D. R. Miller, *Surf. Sci.* **93**, 47 (1980).
- ⁶⁹G. Rovida, M. Torrini, and E. Zanizzi, *Nuovo Cimento B* **4**, 97 (1971).
- ⁷⁰D. G. Castner, G. A. Somorjai, J. E. Black, D. Castiel, and R. F. Wallis, *Phys. Rev. B* **24**, 1616 (1981).
- ⁷¹H. B. Lyon and G. A. Somorjai, *J. Chem. Phys.* **44**, 3707 (1966).
- ⁷²K. Kern, Ph.D. thesis, University Jülich, 1985.
- ⁷³D. R. Hamann, *Phys. Rev. Lett.* **46**, 1227 (1981).
- ⁷⁴A. Lock, diploma thesis, University Göttingen, 1987.
- ⁷⁵J. Ellis, F. Hofmann, and J. P. Toennies (to be published).
- ⁷⁶The classical turning point $z_t = 3.66 \text{ \AA}$ of He above the Ag(001) surface is estimated from the known turning point on Cu(001) (Ref. 75) by a comparison of the corresponding radii of the atomic valence electron densities.
- ⁷⁷G. Armand and P. Zeppenfeld, *Phys. Rev. B* **40**, 5936 (1989).
- ⁷⁸E. Vilallonga and H. Rabitz, *J. Chem. Phys.* **97**, 1576 (1992).
- ⁷⁹The precise nature of the quick scattering approximation used here is to assume that the scattering collision time is short compared to the periods of the predominantly small frequency and long wavelength phonons that dominate the multiphonon exchange.
- ⁸⁰G. G. Bishop, W. P. Brug, G. Chern, J. Duan, S. A. Safran, and J. G. Skofronick, *Phys. Rev. B* **47**, 3966 (1993).
- ⁸¹J. R. Manson, V. Celli, and D. Himes, *Phys. Rev. B* **49**, 2782 (1994).
- ⁸²J. de Launay, in *Solid State Physics*, edited by F. Seitz and D. Turnbull (Academic, New York, 1956), Vol. 2.